Influence of Monsoonal Wind Speed and Moisture Content on Intensity and Diurnal Variations of the Mei-Yu Season Coastal Rainfall over South China

XINGCHAO CHEN

Key Laboratory for Mesoscale Severe Weather, Ministry of Education, and School of Atmospheric Science, Nanjing University, Nanjing, China, and Department of Meteorology, and Center for Advanced Data Assimilation and Predictability Techniques, The Pennsylvania State University, University Park, Pennsylvania, and Center for Prototype Climate Modeling, New York University Abu Dhabi, Abu Dhabi, United Arab Emirates

FUQING ZHANG

Department of Meteorology, and Center for Advanced Data Assimilation and Predictability Techniques, The Pennsylvania State University, University Park, Pennsylvania

KUN ZHAO

Key Laboratory for Mesoscale Severe Weather, Ministry of Education, and School of Atmospheric Science, Nanjing University, Nanjing, China

(Manuscript received 13 March 2017, in final form 14 June 2017)

ABSTRACT

Convection-permitting numerical experiments using the Weather Research and Forecasting (WRF) Model are performed to explore the influence of monsoonal onshore wind speed and moisture content on the intensity and diurnal variations of coastal rainfall over south China during the mei-yu seasons. The focus of the analyses is on a pair of 10-day WRF simulations with diurnally cyclic-in-time lateral boundary conditions averaged over the high versus low onshore wind speed days of the 2007–09 mei-yu seasons. Despite differences in the rainfall intensity, the spatial distributions and diurnal variations of rainfall in both simulations verified qualitatively well against the mean estimates derived from ground-based radar observations, averaged respectively over either the high-wind or low-wind days.

Sensitivity experiments show that the pattern of coastal rainfall spatial distribution is mostly controlled by the ambient onshore wind speed. During the high-wind days, strong coastal rainfall is concentrated along the coastline and reaches its maximum in the early morning. The coastal lifting induced by the differential surface friction and small hills is the primary cause for the strong coastal rainfall, while land breeze enhances coastal lifting and precipitation from evening to early morning. In the low-wind days, on the other hand, coastal rainfall is mainly induced by the land–sea-breeze fronts, which has apparent diurnal propagation perpendicular to the coastline. With stronger land–sea temperature contrast, the land–sea breeze is stronger during the low-wind days. Both in the high-wind and low-wind days, the coastal rainfall intensity is sensitive to the incoming moisture in the upstream oceanic airflow, especially to the moisture content in the boundary layer.

1. Introduction

The coastal region of south China, one of the three biggest population and economic centers in China, is also a center of maximum rainfall during the warm season (Luo et al. 2013; Zheng et al. 2016). Every year, especially from May to June (also called ''mei-yu season of south China''), heavy rainfall events dominate the weather and associated deadly flash floods frequently cause severe property damage over the region (Xu et al. 2009; Wang et al. 2014). Though coastal precipitation has prominent economic and social impacts in this area, it is still an unmet challenge for the numerical models to simulate and predict it accurately, which is at least in part due to our incomplete knowledge of the related physical mechanisms.

With three years (2007–09) of Guangzhou ground-based radar (GZRD) observations, Chen et al. (2015, hereafter C15) investigated the spatial and temporal distributions of rainfall over the south China coastal

Corresponding author: Dr. Kun Zhao, zhaokun@nju.edu.cn

DOI: 10.1175/JAS-D-17-0081.1

region during the mei-yu seasons. Results show that coastal rainfall over the region exhibits a pronounced diurnal cycle, with a maximum in the early afternoon and a secondary peak in the early morning. Precipitation propagates to the ocean from the evening to the early morning and penetrates to the inland area during the afternoon (refer also to Chen et al. 2009; Zhao 2014; Jiang et al. 2017). Using numerical simulations with diurnally cyclic-in-time lateral boundary conditions, Chen et al. (2016, hereafter C16) demonstrated that the mei-yu season diurnal variations of coastal rainfall over the south China coastal region are mainly controlled by the land–sea breeze, which is a localized circulation driven by the diurnally varying differential heating between the land and ocean. The nocturnal offshore rainfall is induced by the convergence line between the onshore monsoonal wind and the land breeze, while the daytime inland-penetrating precipitation is mainly produced by the sea-breeze fronts. Further sensitivity experiments show that cold pool dynamics and costal terrains also exert considerable influences on the intensity and diurnal variability of coastal rainfall over the region.

However, besides the seasonal mean characteristics, the rainfall over the south China coastal region also shows an obvious intraseasonal variability in the mei-yu season. Long-term radar observations show that the coastal rainfall increases substantially when the low-level monsoonal onshore wind becomes stronger (e.g., reaching the criteria of being categorized as a low-level jet with wind speed greater than $12\,\mathrm{m\,s^{-1}}$ in the lower troposphere). Precipitation in the high onshore wind speed days concentrates along the coastline with little diurnal propagation perpendicular to the coastline, which is considerably different from the mean diurnal characteristics of the averaged mei-yu season climatology (Chen et al. 2014, hereafter C14). Obviously, the ambient onshore wind speed is a key parameter controlling the intensity and diurnal variations of the mei-yu season coastal rainfall over south China. We would expect that the diurnally recurring convection produced by the land–sea breeze (or thermally forced circulation) will be suppressed and the mechanically forced coastal rainfall becomes much more important when the large-scale onshore wind speed increases. However, the related processes for such disparity were not examined in C16 but are the main subjects of this study.

In the previous literature, the large-scale wind speed controlling of land–sea-breeze circulation and diurnal rainfall variations has been studied extensively. Analytically, Qian et al. (2009) showed that a sufficiently strong environmental mean flow will lead to the emergence and dominance of a new branch of coastal circulation that is broadly similar to flow past a topographic obstacle (e.g., their Fig. 4), which overshadow and are distinctly different from the classical no-mean-flow sea-breeze circulations as in Rotunno (1983). Qian et al. (2012) further examines the effect of coastal topography on tropical land–sea-breeze circulations under different environmental mean flow conditions. Using long-term TRMM observations, Sobel et al. (2011) found that diurnal cycles of precipitation over small islands are stronger over the Maritime Continent where the ambient wind is weak than over the Caribbean where the ambient wind is strong. Through idealized simulations, Wang and Sobel (2017) further demonstrate that the large-scale wind speed is a crucial factor controlling the diurnal cycles of rainfall over small tropical islands, and the diurnal cycle of rainfall becomes muted when the large-scale wind is high, which is consistent with the earlier idealized study of Qian et al. (2012).

With the data collected from the Hawaiian Rainband Project (HaRP), Esteban and Chen (2008) showed that, with stronger trade winds, rainfall amounts on the windward side of the island of Hawaii will be higher, with the maximum rainfall axis shifts farther inland. Meanwhile, the nocturnal precipitation location is mainly determined by the relative strength between the katabatic flow and the incoming prevailing wind. Similar results can also be found in the modeling study of Yang et al. (2008). The in-situ observations of the Dominica Experiment (DOMEX) showed that, under weak trades, diurnally varying thermally driven convection occurs in the mountains of Dominica with the strongest updraft located over the ridgeline and lee slopes. In contrast, under strong trades, mechanically driven convection occurs over the windward slope of the mountains (Smith et al. 2012). Nugent et al. (2014) studied the transition between thermally and mechanically forced moist orographic convection with the collected data from the DOMEX and numerical simulations. They indicated that the horizontal divergence above the mountains, cloud location, and surface temperature can be used as three indices to quantify such transition in convective forcing in Dominica. Using data from the 2008 Southwest Monsoon Experiment (SoWMEX)/Terrain-influenced Monsoon Rainfall Experiment (TiMREX), Ruppert et al. (2013) compared the diurnal circulations and rainfall in Taiwan during the undisturbed (low onshore wind speed) and disturbed (high onshore wind speed) periods in mei-yu season. They indicated that, during the disturbed period, the strengthened onshore flow and moist environment lead to a reduced flow blocking effect of the inland topographic barrier. As a result, the rainfall was much stronger and shifted to the higher elevations of the Central Mountain Range during the period.

Similar results can also be found in Tu et al. (2014), which studied two heavy localized rainfall events during SoWMEX/TiMREX.

Although some past studies have investigated the influences of ambient wind speed on the land–sea-breeze circulations (Arritt 1993; Zhong and Takle 1993; Atkins and Wakimoto 1997; Zhu and Atkinson 2004; Qian et al. 2009), the detailed dynamic processes and physical mechanisms of the continental coastal rainfall in different ambient onshore wind speed regimes remain largely unexplained and underexplored. Mapes et al. (2003) proposed that diurnal gravity waves driven by daytime heating over elevated coastal terrains are the main mechanism for the offshore propagating coastal precipitation over northwestern South America. However, Qian et al. (2012) challenged such hypothesis using idealized 2D simulations, which showed the inland plateau tends to significantly strengthen the land-breeze part of the circulation by blocking the sea-breeze density current toward land, which in turn produces a stronger land-breeze density current that is likely responsible for offshore propagating precipitation.

Besides the direct dynamical impacts, ambient onshore wind speed also controls the strength of inland transports of oceanic moisture. The intensity and evolutions of convection can be very sensitive to the small perturbations in the environmental moisture (Gilmore et al. 2004; Melhauser and Zhang 2012; Schumacher 2015). The influences of incoming moisture content on coastal rainfall amount and diurnal variations at different ambient onshore wind speeds also need further investigations.

Complimentary to the observational studies of C14 and C15 and the modeling study of C16, numerical simulations with the Weather Research and Forecasting (WRF) Model are conducted in this paper to examine the influences of monsoonal wind speed and moisture content on the intensity and diurnal variations of the mei-yu season coastal rainfall over south China. The spatial distributions and diurnal variations of simulated rainfall are compared with the long-term estimate from radar observations. Through a series of numerical sensitivity experiments, the impacts of land–sea breeze, coastal differential friction, and incoming oceanic moisture on coastal rainfall in different ambient wind speed regimes are investigated. The experimental design is described in section 2. Section 3 presents the ambient wind speed controls of coastal rainfall and impacts of the inland surface drag. The impacts of incoming moisture from the ocean on the coastal rainfall are examined in section 4. Section 5 gives the concluding remarks of the study.

2. Numerical model and experimental design

In C16, the authors used the Advanced Research version of WRF with averaged initial conditions and diurnally cyclic-in-time lateral boundary conditions to simulate the diurnal variations of the land–sea breeze and its related rainfall over the south China coastal region during the 2007–09 mei-yu seasons (11 May–24 June, defined in Xu et al. 2009). The simulation was compared with the averaged estimates from 3-yr ground-based radar observations in the literature to show that the idealized experiment can successfully capture the diurnal cycles of coastal rainfall over the region. In this study, we use the same model configuration as C16 to simulate the diurnal variations of coastal rainfall but with different large-scale onshore wind speeds and moisture content. The Advanced Research version of WRF (Skamarock et al. 2008), version 3.7, is used for this study. Simulations are performed over the south China coastal region, from 19.6° to 26.5°N and from 110.9° to 116.3°E (Fig. 1). The model domain covers most of the south China coastline and is characterized as a plain [Pearl River Delta (PRD)] surrounded by the coastline on the south and moderate-height (400–800 m) mountains to the north. Several small hills (~100 m) can be found close to the coastline. As in C16, the coastline is smoothed using the two-dimensional median filtering with a 160-km (east–west direction) × 40-km (south–north direction) neighborhood size. The inland surface types are prescribed as evergreen broadleaf as a simplification while not losing generality. If the original topography is located over the ocean after the modification of coastline, the topography will be removed and all offshore model grids are prescribed as water. The horizontal grid spacing of the simulations is 4 km and there are 50 stretched-grid vertical levels with a nominal model top at 50 hPa. Vertically propagating gravity waves have been suppressed in the top 5 km of the model with the implicit damping scheme (Klemp et al. 2008). The simulations employ the five-layer thermal diffusion surface model (Skamarock et al. 2008), the Yonsei University (YSU) boundary layer scheme (Hong et al. 2006), the Dudhia shortwave (Dudhia 1989) and Rapid Radiative Transfer Model (RRTM) longwave (Mlawer et al. 1997) radiation schemes, and the WRF single-moment 5-class microphysics scheme (Hong et al. 2004).

During the mei-yu seasons, the prevailing monsoonal wind in the lower troposphere is southerly on average. In C14, the authors found that the southerly wind speed around 2-km height can be used as the indicator of the average onshore wind strength in the low levels. Intense convective rainfall formed along the coastline when a

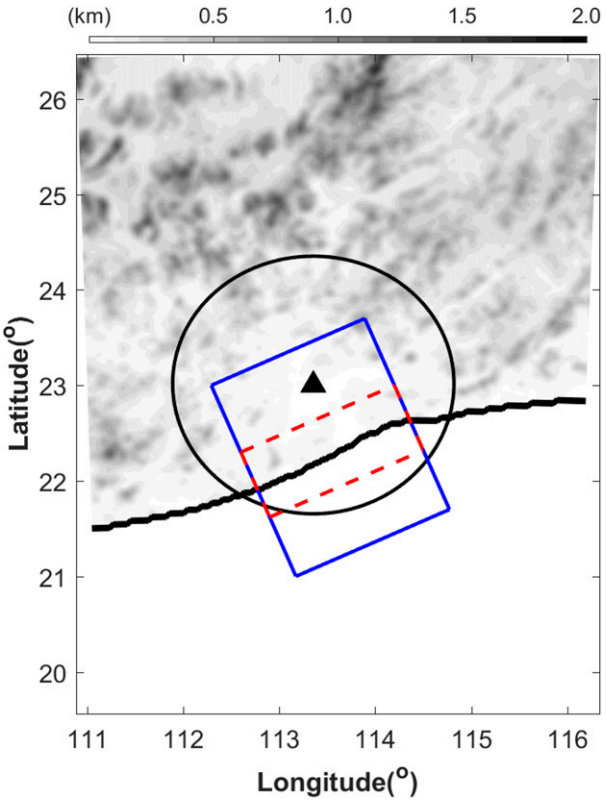

FIG. 1. Model domain and topography with modified coastline. Orography is shown by the grayscale. Location of GZRD is marked by the black triangle and the 150-km observation range of GZRD is shown with a black circle. Coastal region of PRD is shown by the red dashed box.

strong southerly wind appears at this altitude. In this study, using the 0.5°×0.5° operational analysis data from the National Oceanic and Atmospheric Administration (NOAA) Global Forecast System (GFS), we calculate the daily averaged southerly wind speed over the model domain during the 2007–09 mei-yu seasons. All days with a southerly wind at the 2-km altitude are sorted based on the wind strength. The top one-third days are defined as the high-wind days (42 days) and the bottom one-third are defined as the low-wind days (42 days).

The initial and lateral boundary conditions of the simulations are also derived from the 6-hourly GFS 0.5° × 0.5° operational analysis data. As in C16, to capture the general characteristics of coastal rainfall that occurred in the high-wind versus low-wind days during the mei-yu season, the averaged initial and diurnally cyclic-in-time lateral boundary conditions are used in this study. Control experiments HiWind100 and LoWind100 are a pair of 10-day simulations initialized with the 42-day-averaged GFS analysis at 0000 UTC in the high-wind and low-wind days with the 42-day-averaged GFS analysis at 0000, 0600, 1200, and 1800 UTC in the corresponding days as boundary conditions, which cycle periodically in time (i.e., from 0000 to 0600 to 1200 to 1800 UTC and then back to 0000 UTC). With this methodology, simulations can filter out the transient atmospheric perturbations and capture the repeated development of thermally induced diurnal signals such as land–sea breeze within an averaged atmospheric background environment. Besides C16, similar methodology has also been used in many other related works to study the generalized characteristics of different diurnal rainfall processes (Trier et al. 2010; Sun and Zhang 2012; Bao and Zhang 2013; Zhang et al. 2014).

Several sensitivity experiments are designed to further examine the impacts of the differential friction and incoming oceanic moisture on the coastal rainfall amounts at different onshore monsoonal wind speeds. All sensitivity experiments are configured the same as the control experiments HiWind100 and LoWind100, except that the inland roughness length is set equal to that over ocean in HiWindnoDG and LoWindnoDG. In the bulk flux algorithm, surface flux is a function of roughness length. The modification of inland surface roughness length will also reduce the surface heat fluxes over inland region, hence reducing the land–sea thermal contrast. However, this change of land–sea thermal contrast is relatively small in HiWindnoDG and LoWindnoDG, which does not have obvious influence on the land–sea breeze and the coastal precipitation in these two experiments. The water vapor mixing ratios of the initial and lateral boundary conditions are exchanged in HiWindEXqv (high-wind days with the moisture from the low-wind days) and LoWindEXqv (low-wind days with the moisture from the high-wind days), the winds in the boundary conditions are exchanged in HiWindEXwind (same as HiWind100 while the winds in the boundary conditions are changed to that in the low-wind days) and LoWindEXwind (same as LoWind100 while the winds in the boundary conditions are changed to that in the high-wind days), and the water vapor flux on the lateral boundary is reduced to 98%, 95%, and 90% on all model levels for high-wind days (HiWind98, HiWind95, and HiWind90) and low-wind days (LoWind98, LoWind95, and LoWind90), respectively. Further experiments test the sensitivity of water vapor flux (reduction of 2%) only at certain altitudes (i.e., between 0 and 1, between 2 and 3, and between 4 and 5 km) at the lateral boundaries for high-wind days (HiWind98/0–1km, HiWind98/2–3km, and HiWind98/4–5km) and low-wind days (LoWind98/0–1km, LoWind98/2–3km, and LoWind98/4–5km), respectively.

To lessen the sensitivity to model spinup, the first day of each 10-day simulation is excluded in the following

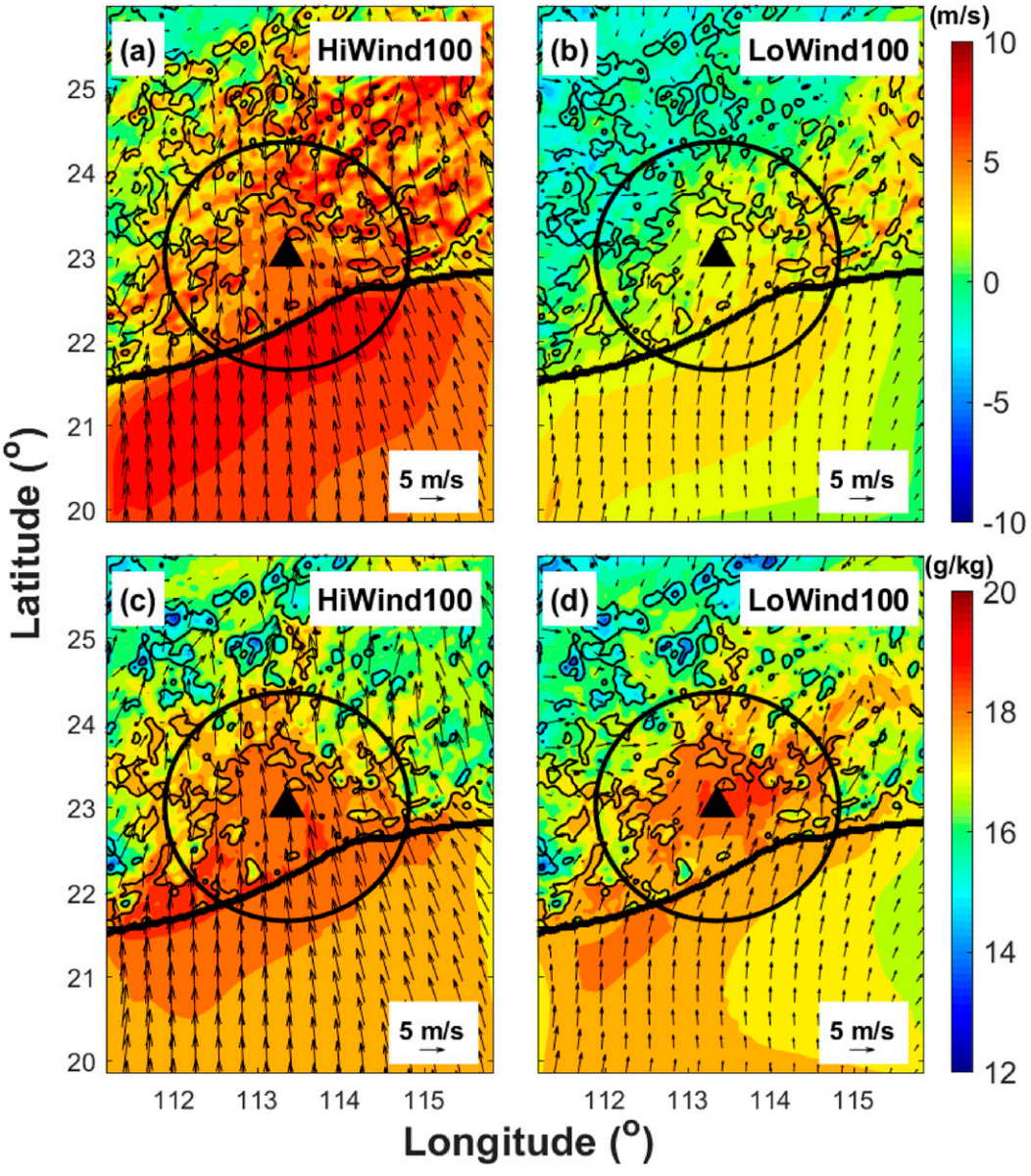

FIG. 2. The average horizontal wind (vectors, m s^{-1}, see reference vector below each panel) at the 0.994-eta level for the final 9 days in the (left) HiWind100 and (right) LoWind100 experiments. Color shadings in (a),(b) are onshore wind speed at the 0.994-eta level. Color shadings in (c),(d) are averaged water vapor mixing ratio below 1 km. Orography is superimposed onto each panel and is shown as black contours that start from 100 m with a 500-m interval.

analyses. All analyses in this study will be focused on the averages of the last 9-day integrations in different experiments.

3. Coastal rainfall under different ambient wind speeds

a. Spatial distributions of rainfall

Figures 2a,b show the mean wind fields at the 0.994-eta level (about 50 m above the surface) averaged for the final 9 days in HiWind100 and LoWind100 with the onshore wind speeds shown in color shadings. Compared to the low-wind days (Fig. 2b), by design, the environmental onshore wind speed near the surface is higher during the high-wind days, which induces stronger horizontal convergence along the coastline (Fig. 2a). The anabatic wind on the windward slope of inland terrains is also stronger during the high-wind days, implying stronger lifting of the incoming oceanic airflow in the inland mountainous area. In the high-wind days, the surface

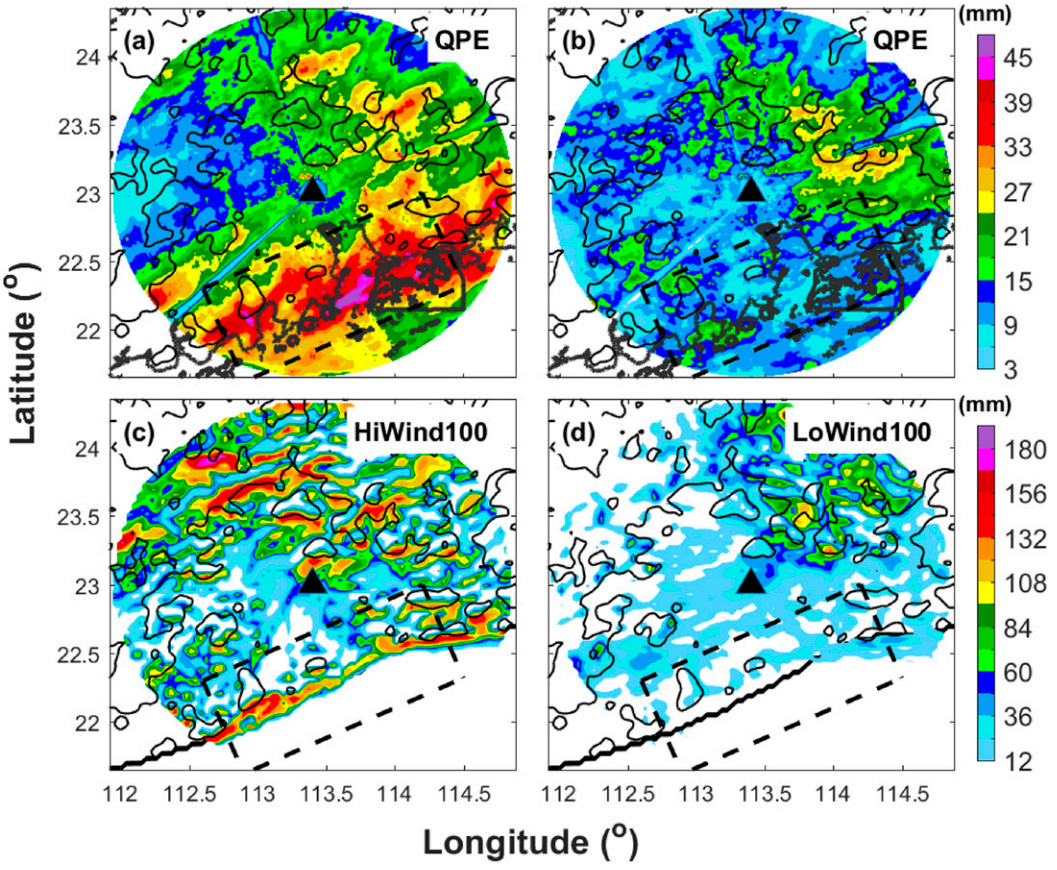

FIG. 3. Spatial distributions of average daily precipitation from GZRD QPE during (a) high-wind and (b) low-wind days and from (c) HiWind100 and (d) LoWind100 experiments. Orography is superimposed onto each panel and is shown as black contours that start from 100 m and have a 500-m interval. Coastal region of PRD is shown by the black dashed box.

wind remains southerly after it across the coastline (Fig. 2a). However, during the low-wind days, the surface wind turns to southwesterly over the inland plain and is lifted by the mountains on the northeast side of the GZRD location (Fig. 2b). The mean water vapor mixing ratios below 1 km in HiWind100 and LoWind100 are shown in color shadings in Figs. 2c and 2d. With stronger shoreward transport of moist oceanic air and horizontal convergence along the coastline, the low-level water vapor mixing ratio near the coastline is considerably higher in HiWind100 than that in LoWind100. Meanwhile, over the inland mountainous area, the low-level water vapor mixing ratios are similar in the two experiments.

The spatial distributions of daily averaged precipitation in HiWind100 and LoWind100 are compared with the quantitative precipitation estimation (QPE) from GZRD over the high-wind and low-wind days, respectively, in Fig. 3. The interested readers can refer to C15 for a detailed description of the radar QPE algorithm. Figures 3a and 3c present the spatial distributions of GZRD-observed and WRF-simulated (HiWind100) daily averaged precipitation during the high-wind days. The dashed black box shows the coastal region (corresponds to the dashed red box in Fig. 1). Both the radar observation and model simulation show a strong precipitation maximum along the coastline in the high-wind days. This is consistent with the descriptions in C14, which demonstrated that the rainfall amount along the coastline increases dramatically when the environmental onshore wind is enhanced. Strong precipitation can also be found at the windward slopes (south slopes) of inland mountains both in the GZRD observations and WRF simulation. However, the rainfall intensity at windward slopes in HiWind100 is noticeably stronger than that in the GZRD observations. Three possible reasons have been given here: First, it may be related to the model's inaccurate representation of atmospheric flow in the mountainous regions, deficiency in the model physics, and/or inadequate resolution, which has also been noticed in other studies focus on the mei-yu rainfall (Chien et al. 2002; Yang et al. 2004). Second, the modified coastal area is narrower than the original one.

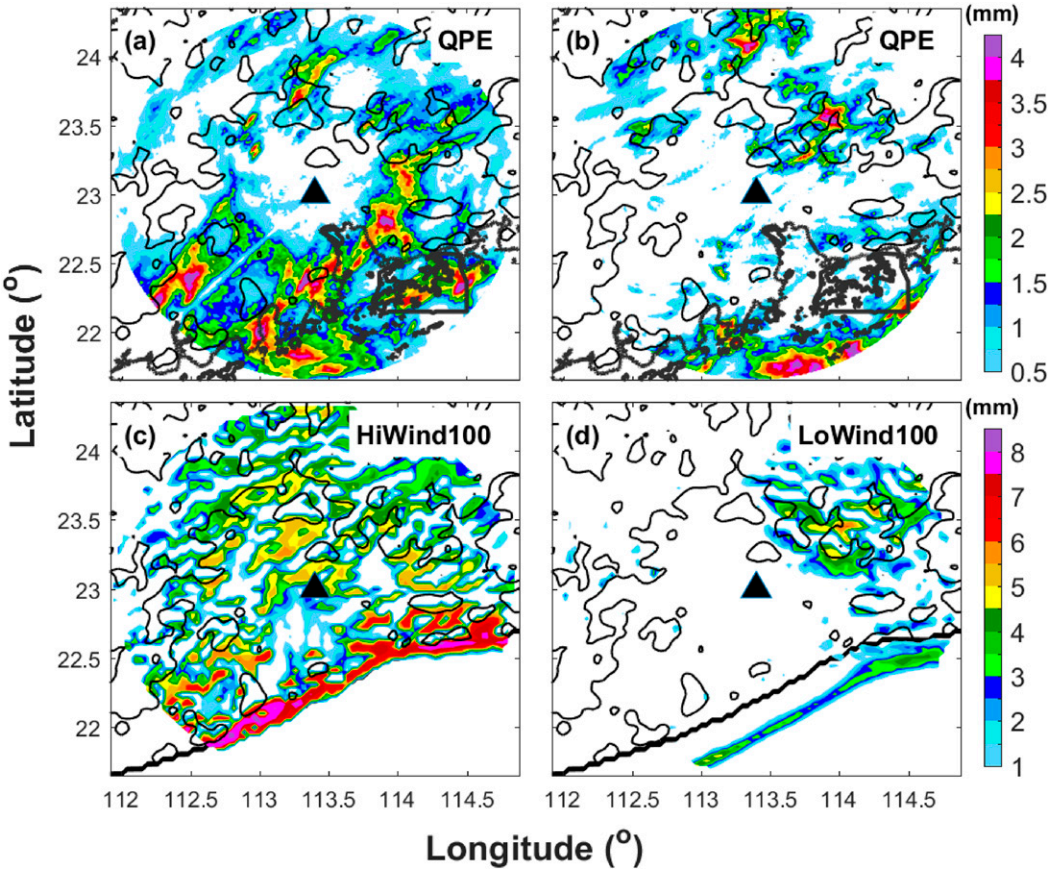

FIG. 4. As in Fig. 3, but for hourly precipitation between 0700 and 0800 LST.

Consequently, rain triggering is less and precipitation is mostly concentrated along the smoothed coastline. More water vapor can be transported into the inland mountainous area and lifted by the orography. Third, radar QPE may also underestimate the precipitation over complex terrain (Wang et al. 2016). Thus, one should not expect the simulated rainfall to match exactly with the radar observational estimate. Nevertheless, despite differences in the rainfall intensity, the simulation can successfully capture the spatial distributions of precipitation, especially over the coastal region, which is the focus of this study. In contrast with the high-wind days, precipitation along the coastline turns to be very weak during the low-wind days (Figs. 3b and 3d). Only one inland rainfall maximum located at the windward slopes of the northeast mountainous area can be found in the GZRD observations (Fig. 3b) and LoWind100 (Fig. 3d), which corresponds to the orographic lifted low-level southwesterly wind from the plain during the low-wind days (Fig. 2d).

b. *Diurnal cycles of rainfall*

Besides the spatial distributions of daily averaged precipitation, the diurnal variations of simulated rainfall in HiWind100 and LoWind100 are also compared with the counterparts in the GZRD observations quantitatively. Figures 4a and 4c show the spatial distributions of GZRD-observed and WRF-simulated averaged precipitation between 0700 and 0800 LST during the high-wind days. The land-breeze reaches its strongest phase during this hour in the mei-yu season (C16). Despite the overprediction of the inland rainfall in HiWind100, we can find that, both in the GZRD observations and WRF simulation, strong precipitation is concentrated around the coastline at this hour. However, during the low-wind days, precipitation over the coastal region is weak (Figs. 4b and 4d). Instead, an offshore rainfall line forms over the open ocean area. In C16, the authors indicate that this offshore rainfall line is induced by the convergence between the prevailing low-level onshore monsoonal wind and the land breeze in the early morning. A small inland rainfall center can also be found at the windward slopes of the northeast mountainous area in the low-wind days, which is closely related to the nocturnal acceleration and enhanced lifting of the southwesterly boundary layer flow from the plain (C15).

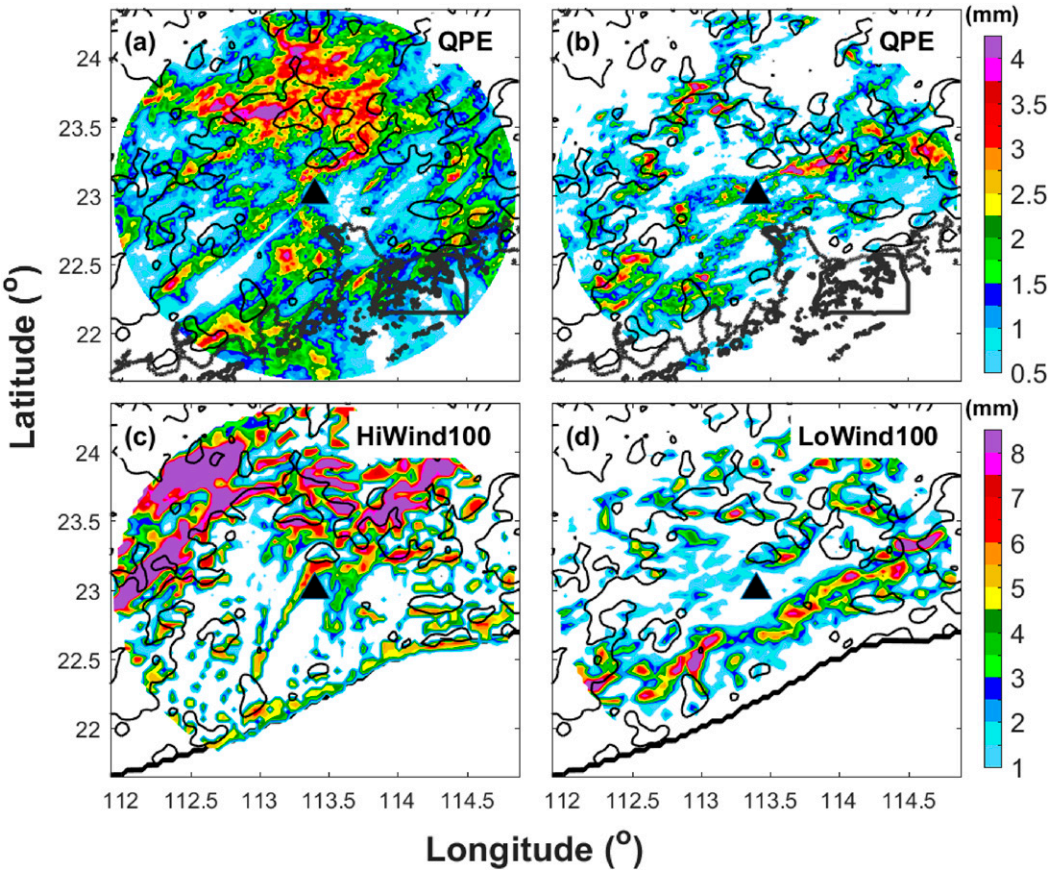

FIG. 5. As in Fig. 4, but for between 1500 and 1600 LST.

Figure 5 shows the spatial distributions of GZRD-observed and WRF-simulated averaged precipitation between 1500 and 1600 LST in the high-wind and low-wind days. The sea breeze reaches its strongest phase in this hour during the mei-yu season (C16). Both in the simulation and observation, strong precipitation can be found over the inland mountainous regions during this hour in the high-wind days (Figs. 5a and 5c). This inland rainfall maximum is closely related to the solar heating effect and the upslope wind of the daytime mountain–plain solenoids (MPS; He and Zhang 2010; Bao and Zhang 2013). Meanwhile, an apparent precipitation maximum can still be found along the coastline in the high-wind days, but the rainfall intensity is weaker than that in the early morning (Figs. 4a and 4c). In the high-wind days, this coastal rainfall maximum is quasi stationary with little diurnal propagation perpendicular to (and away from) the coastline. In contrast, during the low-wind days, rainfall in the mountainous regions is much weaker between 1500 and 1600 LST. Both the radar observation and WRF simulation show a clear line of rainfall maximum associated with the sea-breeze front propagating to the inland area during this hour (Figs. 5b and 5d).

The inland-penetrating speed of this rainfall line in LoWind100 is slightly slower than the counterpart in the GZRD observation, which may be due to the modification of the coastline in the idealized experiment that removes the Pearl River Bay located at the center of the domain to eliminate the complicating influences by the bay breeze. Generally speaking, the WRF simulations can successfully capture the spatial distributions and diurnal variations of precipitation in the high-wind and low-wind days, with timing and location similar to the radar observations: during the high-wind days, there is a quasi-stationary coastal rainfall maximum with little propagation away from the coastline, while diurnal variations of the coastal rainfall intensity can still be found. On the other hand, the accumulated coastal rainfall amount in the low-wind days is much lower. Precipitation over coastal region is mainly induced by the land–sea-breeze fronts, which propagate offshore during the nighttime and penetrate to the inland areas during the daytime.

Strong ambient onshore wind not only suppresses the rainfall produced by the land- and sea-breeze fronts but also modifies the land–sea-breeze circulations

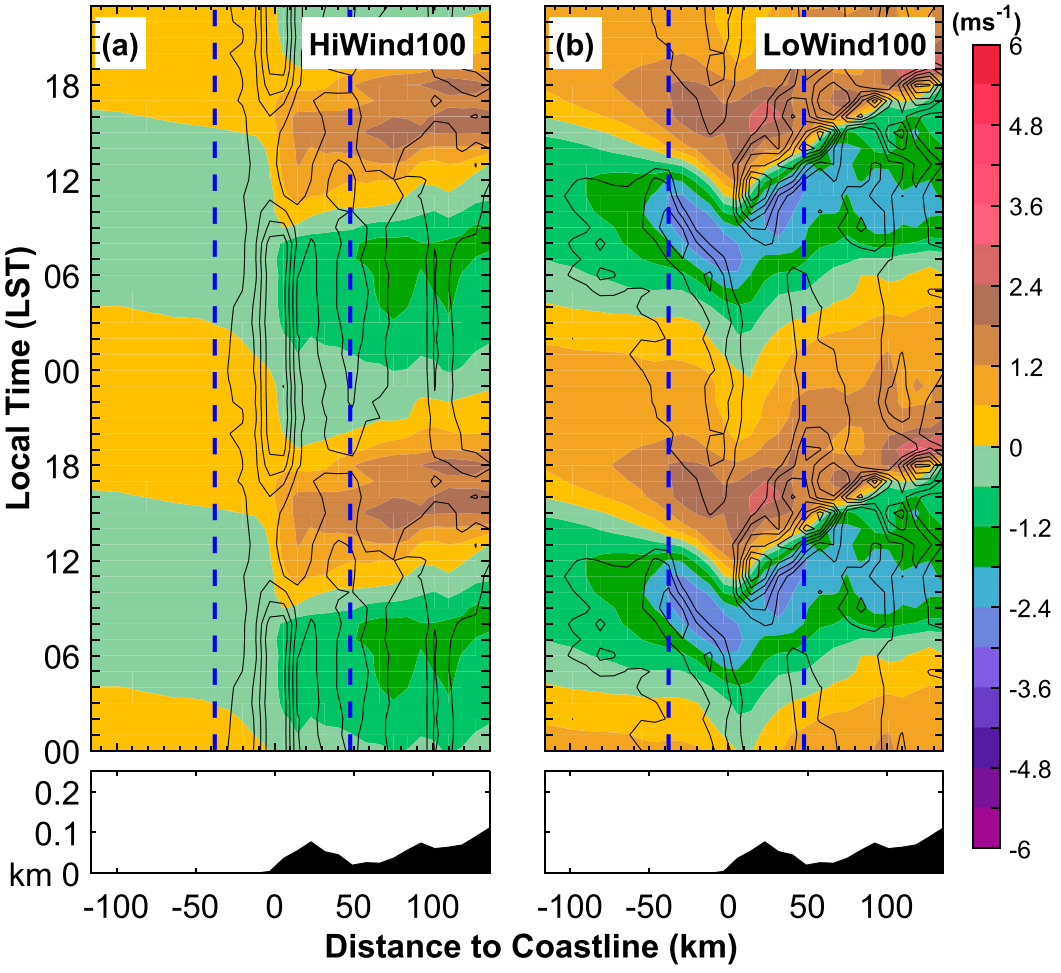

FIG. 6. Hovmöller diagrams of horizontal divergence perpendicular to the coastline (black contours that start from $-1 \times 10^{-5}\,s^{-1}$ and have a $-5 \times 10^{-5}\,s^{-1}$ interval) and perturbation onshore wind (color shadings) at the 0.994-eta level along the long axis of the blue box in Fig. 1 and averaged along the short axis of this box in (a) HiWind100 and (b) LoWind100 experiments. The average topographic profiles are shown by the black shading below each panel. The coastal region of PRD is shown by the blue dashed lines.

(Qian et al. 2009). To elucidate the impacts of the ambient onshore wind speed on the diurnal variations of the land–sea breeze, the Hovmöller diagrams of perturbation onshore wind speed at the second lowest WRF (0.994 eta) level in HiWind100 and LoWind100 are shown in Fig. 6. The average daily mean wind has been subtracted to reveal more clearly the diurnal cycles of the coastal circulations. The horizontal divergence perpendicular to the coastline at the 994-eta level is further superimposed in black contours. Both Hovmöller diagrams are along the long axis of the blue box shown in Fig. 1 and averaged along the short axis of the box. Blue dashed lines show the coastal region which corresponds to the dashed red box shown in Fig. 1.

Clear land- and sea-breeze circulations can be found both in HiWind100 and LoWind100 (Fig. 6). In the high-wind days (Fig. 6a), the land breeze begins to establish on the coastline around 2000 LST and quickly expands to the inland areas after the establishment. However, the land breeze has little offshore expansion and the ocean area is still occupied by the sea breeze between 2000 and 0400 LST, which indicates that the offshore propagation of the land breeze is suppressed by the strong environmental onshore wind during these 6 h. Such large-scale wind cancelation of the land–sea-breeze propagation has also been found in the idealized two-dimensional simulations (Bechtold et al. 1991) and the analytical study of Qian et al. (2009). After 0400 LST, the land breeze becomes strong enough to conquer the environmental obstacle and expands to the ocean area. The perturbation wind direction over the ocean area is reversed to the onshore direction. The sea breeze begins to establish at the coastline from 0930 LST and expands farther inland then with a propagating speed around

$9.0\,m\,s^{-1}$. Similar to the land breeze, the offshore expansion of the sea breeze also has a 6-h lag in the inland intrusion, which is suppressed by the strong environmental shoreward wind. Meanwhile, the offshore parts of the land–sea breeze are also much weaker than the onshore parts during the high-wind days.

Strong horizontal convergence can be found along the coastline in Fig. 6a, which explains why there is a prominent precipitation maximum over the coastal region during the high-wind days: moist air parcels transported from the ocean are forced to rise on the coastline and produce more intense rainfall here. The lifting effect of coastal small hills or/and the differential friction between the ocean and inland surface could be the possible physical reasons of the enhanced coastal convergence, which will be discussed in detail in section 3c.

Corresponding to the diurnal variations of coastal rainfall intensity shown in Figs. 4 and 5, the coastal convergence is stronger during the nighttime, leading to the strongest coastal rainfall in the early morning. Compared with the convergence induced by coastal terrains, the horizontal convergence along the land- and sea-breeze fronts is much weaker in HiWind100, which explains why there is little diurnal propagation of rainfall perpendicular to the coastline during the high-wind days.

As in HiWind100, a clear land–sea-breeze circulation can also be found in LoWind100 (Fig. 6b). However, obvious differences can also be found: first of all, the land–sea breeze is much stronger and the establishing times of land- and sea-breeze circulations are later during the low-wind days (Fig. 6b), which are consistent with findings in the two-dimensional nonlinear numerical simulations (Arritt 1993). The land breeze begins to establish at the coastline from 0000 LST and the establishment of sea breeze is around 1200 LST during the low-wind days, which are similar to the average land–sea-breeze establishment times during an averaged meiyu season (C16). Second, at weak environmental wind speed, the ambient onshore wind is not strong enough to counter the offshore propagation of the land–sea breeze after its establishment. In LoWind100, the onshore- and offshoreward expansions of the land–sea breeze occur simultaneously, with an inland propagating speed close to $5.3\,m\,s^{-1}$. The offshore part of the land breeze is stronger than its onshore part and the onshore part of the sea breeze is stronger than its offshore part. Third, the horizontal convergence associated with the land- and sea-breeze fronts are much stronger than that along the coastline during the low-wind days, which implies that there are potent updrafts along/ahead of the frontal surfaces and precipitation is produced near the fronts. Consequently, the precipitation has apparent propagation in the directions perpendicular to the coastline, while the accumulated rainfall amount in the coastal region is relative smaller during the low-wind days, as described in Figs. 3–5.

To further illustrate the impacts of ambient onshore wind speed on the diurnal variations of the land- and sea-breeze circulations, the cross sections perpendicular to the coastline in HiWind100 and LoWind100 are presented in Figs. 7 and 8. As in Fig. 6, all cross sections in Figs. 7–8 have the same horizontal spatial dimension, which is along the long axis of the blue box shown in Fig. 1 and averaged along the short axis of the box. The cross section of the mean wind vectors perpendicular to the coastline (arrows) and mean onshore wind speed (color-filled contours) in HiWind100 is shown in Fig. 7a. During the high-wind days, the prevailing onshore wind is strong. The mean onshore wind speed in the boundary layer is around $7\,m\,s^{-1}$ and decreases gradually with height. The whole lower troposphere is dominated by an onshore wind. Air from the ocean is forced to rise near the coast, which corresponds to the horizontal convergence along the coastline shown in Fig. 6a.

Figures 7b–i shows the cross sections (at 3-h intervals) of perturbation wind vectors and speed perpendicular to the coastline and the temperature perturbations in HiWind100. Because the heat capacity of land is much smaller than that of ocean, strong diurnal temperature perturbations (>1 K) can only be found over the inland regions in Fig. 7. This land–sea temperature contrast induced by the different heat capacities is the essential driving force of the land–sea-breeze circulations. At 0000 LST, the whole region is still featured as an onshore perturbation wind below 3 km (Fig. 7b), which is a combined signal of the residual sea breeze and the diurnal cycle of regional monsoon flow (Chen et al. 2013), or even the planetary-scale sea breeze (Huang et al. 2010). Only the wind in the lowest 100-m levels on the inland side of the coastline has changed to a land breeze (Fig. 6a). At 0300 LST, with the decrease of inland surface temperature, the land breeze becomes stronger and clear signal of offshore perturbation wind can be found over the coastal region (Fig. 7c). The thickness of land breeze is also increased but still below 500 m.

In the early morning (0600 LST), the wind in the lowest 2-km levels has changed to an offshore wind except for the north slopes of the coastal hills, which may be related to the downslope wind of the nighttime MPS circulation of the hills (Fig. 7d). The land breeze reaches its strongest stage at this time. However, with the weak land–sea temperature contrast, the land-breeze circulation in the high-wind days is weak and is separated into two parts by the MPS circulations induced by small coastal hills. The inland temperature

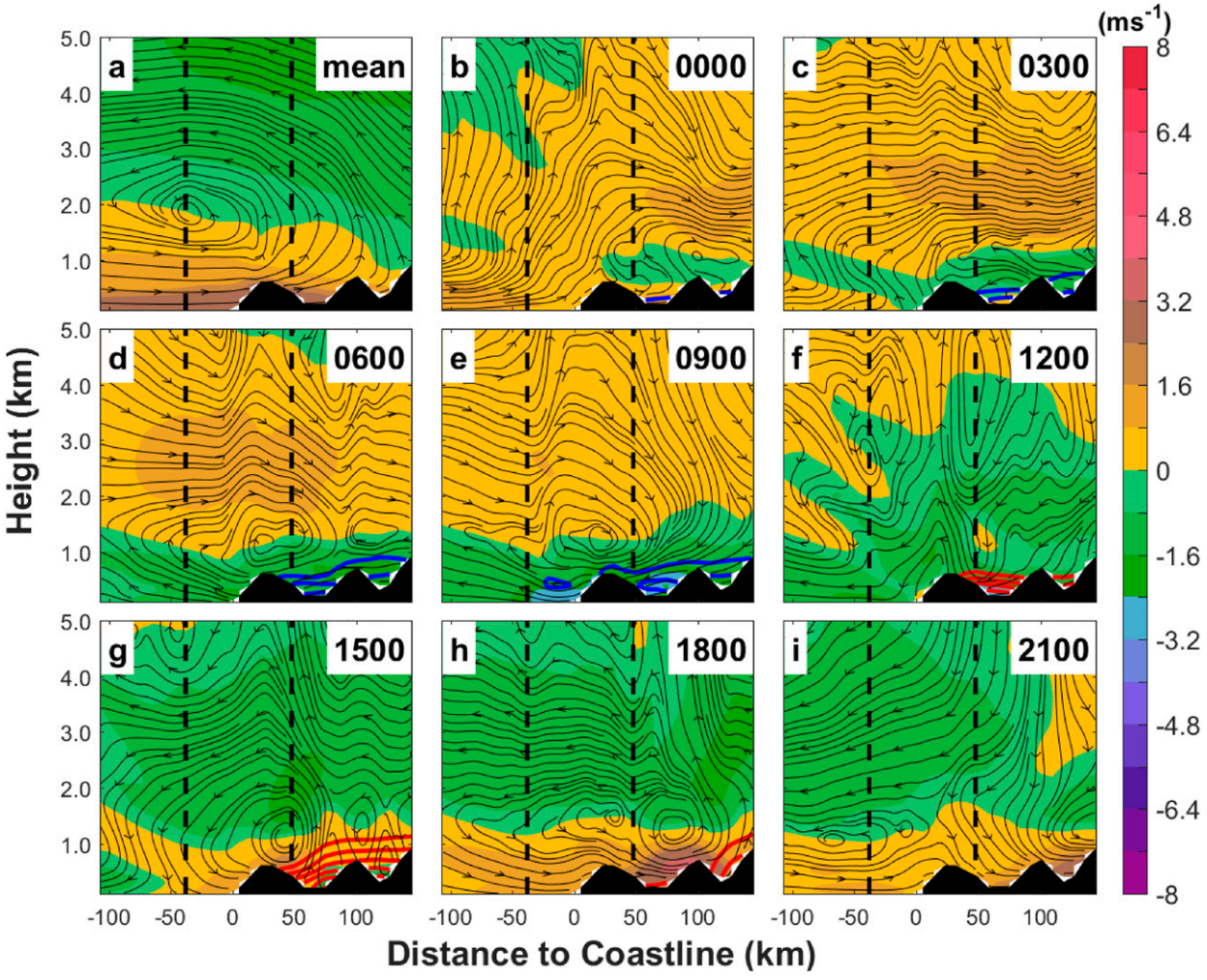

FIG. 7. (a) Cross section of mean wind vectors (streamlines) and onshore wind (color shadings); and cross sections of perturbation wind vectors (streamlines) and onshore wind (color shadings) at (b) 0000, (c) 0300, (d) 0600, (e) 0900, (f) 1200, (g) 1500, (h) 1800, and (i) 2100 LST from the HiWind100 experiment. All cross sections are along the long axis of the blue box in Fig. 1 and averaged along the short axis of this box. The highest topographic profilers along the long axis of the blue box in Fig. 1 are shown by the black shading. Positive perturbation temperature is shown by the solid red contours (that start from +1 K and have a 0.5-K interval) and negative ones are shown by the solid blue contours (that start from −1 K and have a −0.5-K interval).

increases with the solar heating in the morning (Fig. 7e). As a result, the land-breeze circulation becomes unapparent by 0900 LST. At 1200 LST, the sea breeze is established over the coastal region, but concentered in the lowest 100-m levels (Figs. 7f and 6b). The lower troposphere is still occupied by an offshore perturbation wind, which is a combination of the residual land breeze and the diurnal cycle of regional monsoon flow, or planetary-scale land breeze. The sea breeze becomes thicker and stronger in the next 3 h (Fig. 7g). At 1500 LST, the inland regions are mainly occupied by the onshore perturbation wind in the lowest 2-km levels with a counter clockwise circulation found in the inland areas. The offshore propagation of the sea breeze is suppressed by the strong environmental onshore wind and the open ocean is still prevailed by offshore perturbation flow. The whole lower troposphere turns to an onshore wind at 1800 LST, which shows a combined signal of sea breeze and the diurnal cycle of large-scale flow (Fig. 7h). Two sea-breeze circulations can be found over the ocean and inland regions separately. The inland part of the sea-breeze circulation is stronger than the offshore part. During the evening hours (Fig. 7i), the lower troposphere of the cross section is still dominated by an onshore perturbation wind while a land-breeze circulation begins to establish along the coastline in the lowest 100 m (Fig. 6a).

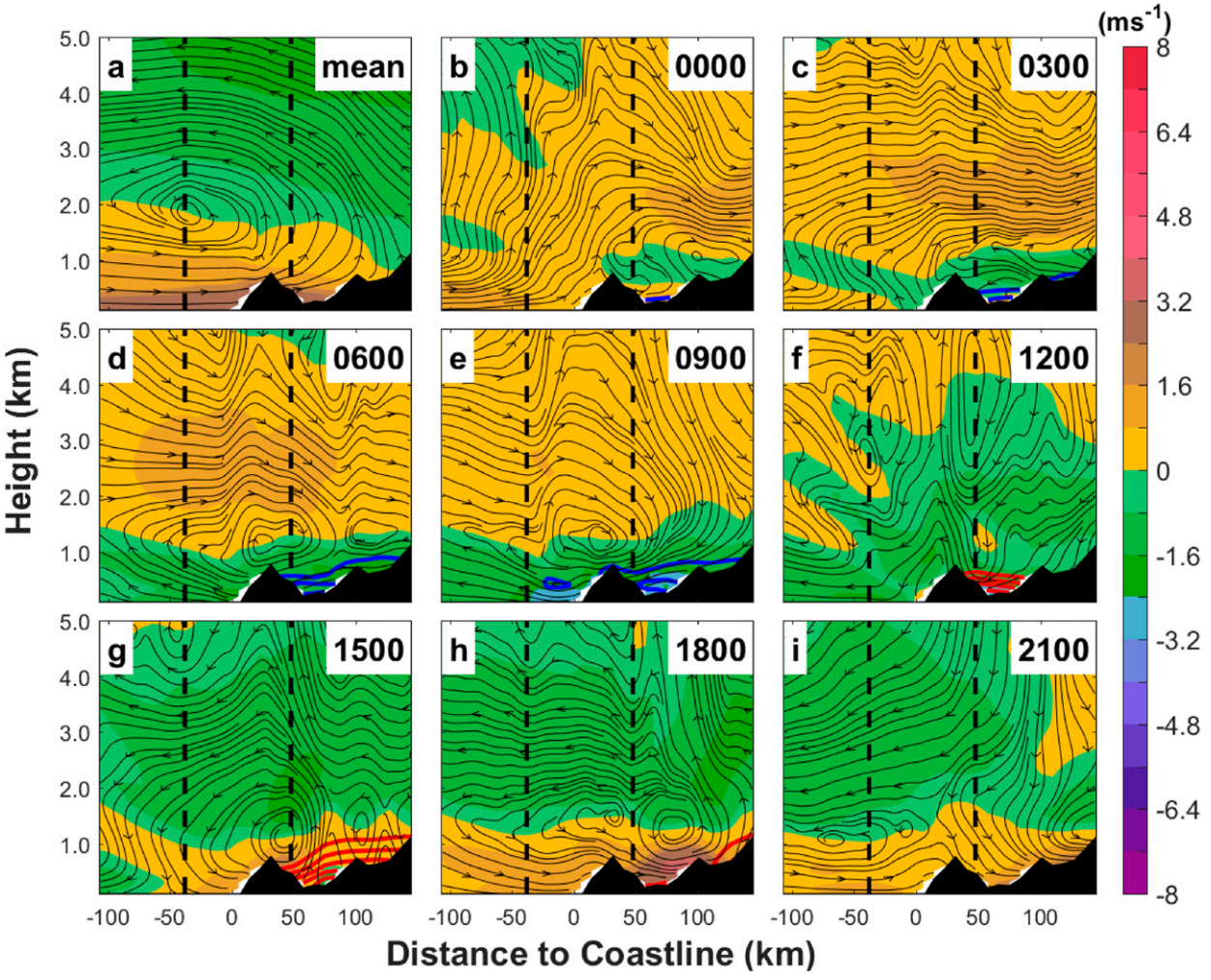

FIG. 8. As in Fig. 7, but from LoWind100 experiment.

Figure 8a shows the cross section of mean wind vectors perpendicular to the coastline and the mean onshore wind speed in LoWind100. In the low-wind days, a counterclockwise circulation across the coastline can be found in the troposphere. The low-level onshore wind speed is much slower than that in the high-wind days, with the prevailing wind turning to the offshore direction above the 2-km height. The onshore wind speed in the boundary layer is around $3\,m\,s^{-1}$ in LoWind100, which is slower than the $7\,m\,s^{-1}$ in HiWind100. This prevailing onshore wind speed difference ($4\,m\,s^{-1}$) is likely the reason for a slower inland propagation of land–sea breeze in the low-wind days (around $5.3\,m\,s^{-1}$) than that in the high-wind days (around $9.0\,m\,s^{-1}$). Stronger ambient onshore wind pushes the land- and sea-breeze circulations into the inland areas faster.

During the low-wind days, the lower troposphere is also featured as an onshore perturbation wind at 0000 LST while an offshore perturbation wind can be found over the inland basin above the residual sea breeze, which is featured by a katabatic flow from the farther inland mountainous areas (C16). The land breeze begins to establish in the lowest 100-m levels along the coastline at this time. In the next 6 h, the land breeze becomes stronger and then expands farther inland and offshore (Figs. 8c and 8d). At 0600 LST, the sea breeze reaches its strongest stage and the whole lower troposphere is featured as an offshore perturbation wind (Fig. 8d). The offshore perturbation wind is shallower than that in HiWind100, which may be related to the decline of the diurnal variation of regional monsoon flow in the low-wind days (Chen et al. 2013). With a larger land–sea surface temperature contrast, the land-breeze circulation in LoWind100 is much stronger and deeper than that in HiWind100. In LoWind100, the land-breeze circulation is featured as a clockwise circulation across the coastline, with the updraft over the ocean and downdraft over the inland regions. The land-breeze circulation is

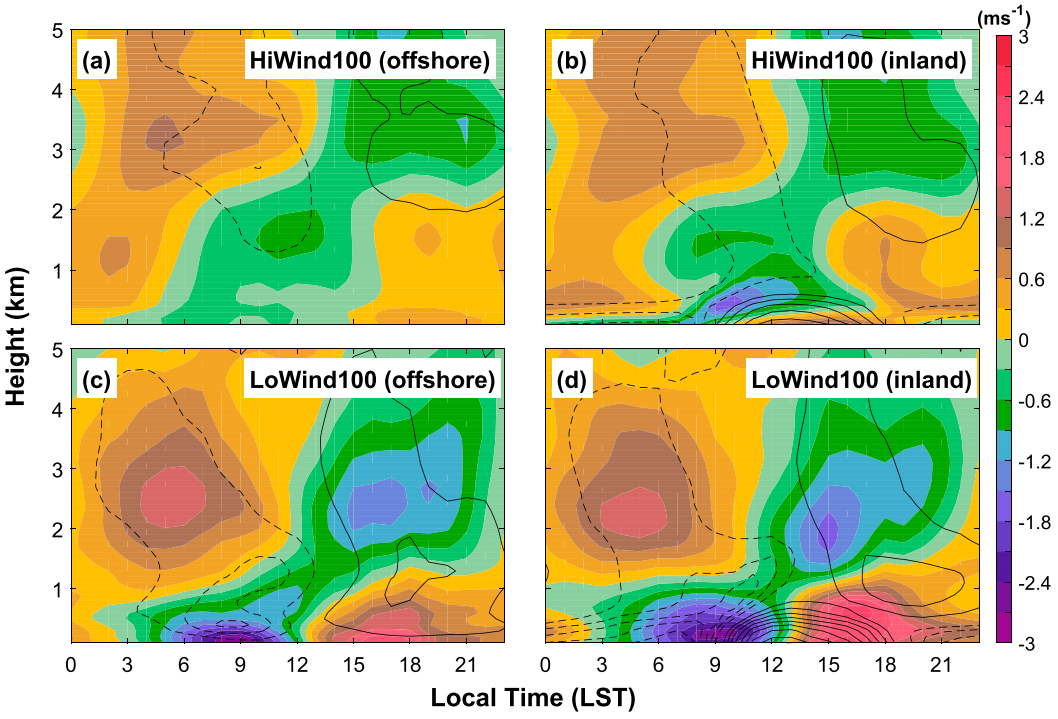

FIG. 9. Diurnal variations of vertical profiles of perturbation onshore wind (color shading) and temperature [black contours; positive (negative) perturbation temperatures are solid (dashed); contour interval is 0.3 K] over the (a),(c) offshore and (b),(d) inland subregions of coastal region (shown by the red dashed box in Fig. 1) in the (top) HiWind100 and (bottom) LoWind100 experiments.

still distinguishable until 0900 LST with strong negative perturbation temperature over the inland regions (Fig. 8e). At noontime, with enhancement of the solar heating effect, the inland perturbation temperature turns positive (Fig. 8f). A shallow onshore wind and weak counterclockwise circulation appear near the coastline, which are the combination of newly established sea breeze and the upslope wind of coastal hills. The sea breeze becomes stronger and expands farther inland and offshore in the next 3 h and reaches its strongest stage at 1500 LST. The depth of the mature sea-breeze circulation is similar to that of the land-breeze circulation in the low-wind days, with the downdraft over the ocean and updraft over the inland region. At 1800 LST, the sea-breeze circulation is still present, with the inland counterclockwise circulation is strengthened by the upslope wind of the inland MPS. The sea-breeze circulation decays during the evening hours (around 2100 LST), while the lower troposphere is still featured as an onshore perturbation wind which is shallower than that in the high-wind days (Figs. 8i and 7i).

Overall, the land- and sea-breeze circulations during the low-wind days (LoWind100) are much stronger and deeper than that in the high-wind days (HiWind100), which is closely related to the stronger land–sea temperature contrast in the low-wind days. Meanwhile, the strength of the diurnal variation of large-scale monsoonal flow is weaker during the low-wind days, which is similar to Chen et al. (2013).

To reveal more clearly the diurnal cycles of land–sea breezes near the coast, the diurnal variations of perturbation onshore wind and perturbation temperature in HiWind100 and LoWind100 are further shown in Fig. 9. The coastal region shown in Fig. 1 (red dashed box) has been separated into the offshore and inland subregions based on their underlying surface types. The hourly perturbation wind and temperature are averaged over these two subregions respectively. As shown in Fig. 6, clear land–sea-breeze signals can be found both over the offshore and inland subregions in HiWind100 and LoWind100. With different heat capacities, the diurnal perturbation temperatures over the inland subregion are more obvious than that over the offshore subregion in the boundary layer (Figs. 9b and 9d vs Figs. 9a and 9c). As in the analysis of Figs. 7–8, the inland diurnal perturbation temperature in the low-wind days (Fig. 9b) is stronger and deeper than that in the high-wind days (Fig. 9d). As a result, the land–sea-breeze circulations in LoWind100 are much stronger and deeper than that in HiWind100, over both the inland and offshore subregions. The transition time from negative to positive inland

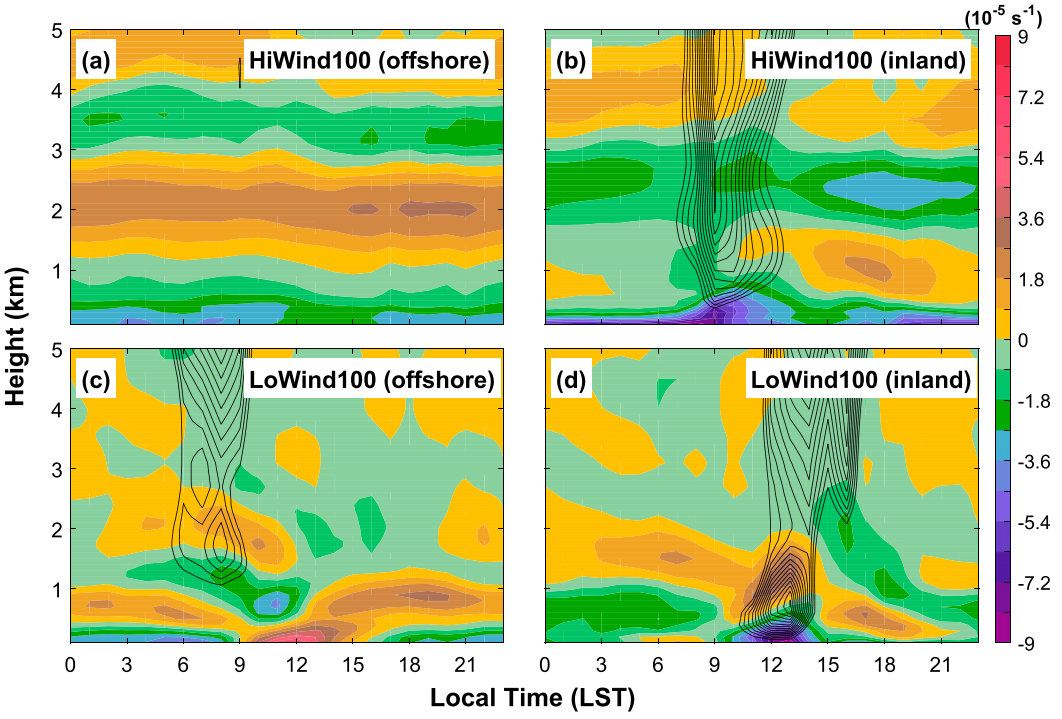

FIG. 10. As in Fig. 9, but for horizontal divergence perpendicular to the coastline (color shading) and the positive perturbation vertical velocity (black contours with interval of 0.01 m s^{-1}).

perturbation temperatures is similar in HiWind100 and LoWind100 (Figs. 9b and 9d), which reflects that the diurnal cycles of solar heating are similar in the high-wind and low-wind days. However, as shown in Fig. 6, the transition time from the land to sea breeze on lowest model levels in LoWind100 is later than that in HiWind100, which can be explained as the diurnal variations in the low-wind days are stronger and consequently harder to be reversed (Fig. 9d). Consistent with the analysis of Fig. 6, in the high-wind days, the transition time from the land to sea breeze over the offshore subregion is also later than that over the inland subregion (Figs. 9a and 9b), while the transition time in two subregions are similar during the low-wind days (Figs. 9c and 9d).

Figure 10 shows the diurnal variations of horizontal divergence and positive perturbation vertical velocity averaged over the offshore and inland subregions in Hiwind100 and Lowind100. During the high-wind days, the strong large-scale onshore wind induces a strong horizontal convergence near the coastline in the low levels (Figs. 10a and 10b), which produces intense coastal precipitation over the coastal region (Figs. 3a and 3c). Because the offshore part of the land–sea breeze is weak during the high-wind days, we can find there are little diurnal variations of vertical velocity over the offshore subregions. In contrast, over the inland subregions, the land breeze enhances the low-level convergence considerably during the nighttime and induces a stronger updraft in the early morning (Fig. 10b), which corresponds to the enhancement of coastal rainfall in the early morning during the high-wind days (Figs. 4a and 4c). In the low-wind days, on the other hand, the low-level convergence over the coastal region is weaker on average but has more obvious diurnal cycles. Over the offshore subregions, the low-level horizontal convergence is enhanced by the land breeze in the early morning and induces a stronger updraft (Fig. 10c) and offshore rainfall during the time (Figs. 4b and 4c). Meanwhile, from noon to the early afternoon, the sea breeze induces a low-level divergence over the offshore subregion in the low-wind days. In contrast, over the inland subregion, the lowest levels turn divergence in the early morning when the land breeze reaches its strongest stage (Fig. 10d). From noon to the early afternoon, the sea breeze enhances the low-level convergence over the inland subregion considerably and induces a stronger updraft and precipitation over the coastal region (Fig. 6b).

c. *Effects of differential friction*

In C14, with the surface and radar radial velocity observations, the authors hypothesized that lifting of the incoming oceanic air parcels induced by the differential surface friction between the land and ocean is the

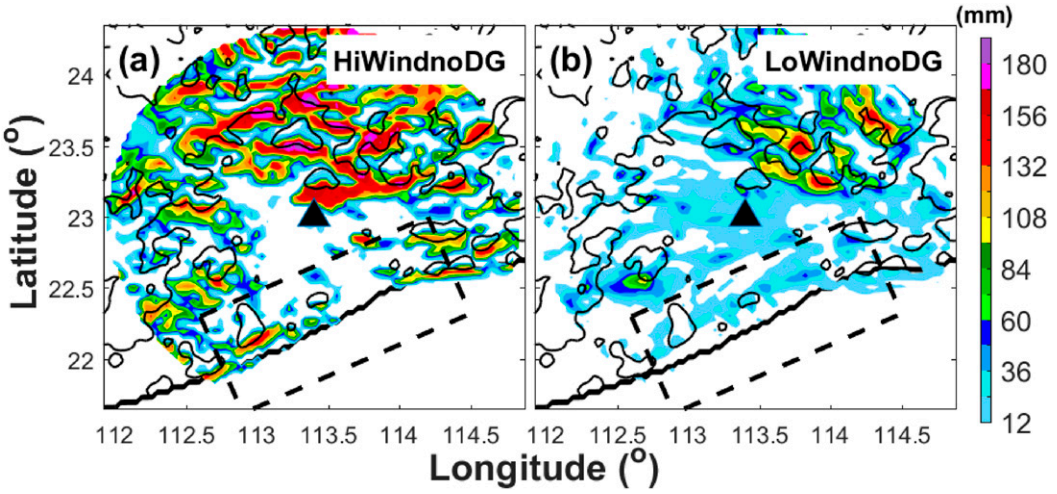

FIG. 11. Spatial distributions of average daily precipitation from (a) HiWindnoDG and (b) LoWindnoDG experiments. Orography is superimposed onto each panel and is shown as black contours that start from 100 m and have a 500-m interval. Coastal region of PRD is shown by the black dashed box.

primary cause of the coastal rainfall maximum in the high-wind days. To investigate to what extent the inland surface drag can influence the coastal rainfall amount at different onshore wind speeds, two sensitivity experiments HiWindnoDG and LoWindnoDG are conducted in this study, with the roughness length of the inland model grids set equal to that over ocean (roughness length Z_0 = 0.01 m). Figure 11 shows the spatial distributions of the daily averaged precipitation in HiWindnoDG and LoWindnoDG. Compared with HiWind100, the accumulated rainfall along the coastline reduces considerably in HiWindnoDG (Fig. 11a). Most rainfall is concentrated on the windward slopes of the small coastal hills in HiWindnoDG. The total rainfall amount over the coastal region reduces to 46% of that in HiWind100. The results illustrate that both the differential surface friction and the lifting of small coastal hills are crucial to the enhancement of coastal rainfall in the high-wind days, with nearly half the total coastal rainfall amount coming from the inland surface drag effect. Sensitivity experiments to the small coastal hills show that the rainfall enhancement induced by the small hills is close to that induced by the differential surface friction, with the enhanced precipitation mainly concentrated on the windward slopes of the small hills (not shown here). Similar results have also been documented in another study on the coastal rainfall enhancement over Long Island in New York (Colle and Yuter 2007). With the decrease of coastal rainfall, an increase of inland precipitation over the mountainous regions can also be found in HiWindnoDG. This inland rainfall enhancement can be explained as follows: without the coastal convergence induced by the differential surface friction, more moist air from the ocean can be transported to the inland area and lifted by the inland mountains. During the low-wind days, the coastal rainfall amount is almost unchanged after the inland surface drag is reduced (Fig. 11b). When compared with LoWind100, the total rainfall amount in LoWindnoDG is only reduced by 7%. Similar results can also be found in the sensitivity experiments to the small coastal hills; the influence of the small hills on the total rainfall amount is very limited in the low-wind days (not shown here). This reflects that the precipitation produced by the land–sea-breeze fronts under the weak ambient wind speed is nearly unaffected by the differential surface friction between the ocean and land and the small coastal hills.

The Hovmöller diagrams of perturbation onshore wind speed and horizontal divergence perpendicular to the coastline at the 0.994-eta level in HiWindnoDG and LoWindnoDG are shown in Fig. 12. We can find that the diurnal variations of the land–sea breeze in HiWindnoDG and LoWindnoDG are similar to those in HiWind100 and LoWind100, with the establishing time of land–sea breeze in LoWindnoDG 1 h later than that in LoWind100. In HiWindnoDG, the horizontal convergence along the coastline is dramatically reduced after the inland surface drag is reduced, which leads to a weaker coastal rainfall (Fig. 12a). Consequently, more moist air parcels transported from the ocean are lifted by the coastal hills and stronger rainfall occurs at the windward slope of the coastal hills in HiWindnoDG (Fig. 11a). In contrast, in LoWindnoDG, the convergence along the land- and sea-breeze fronts has no obvious change after the modification of inland surface drag, suggesting that the impact of differential surface

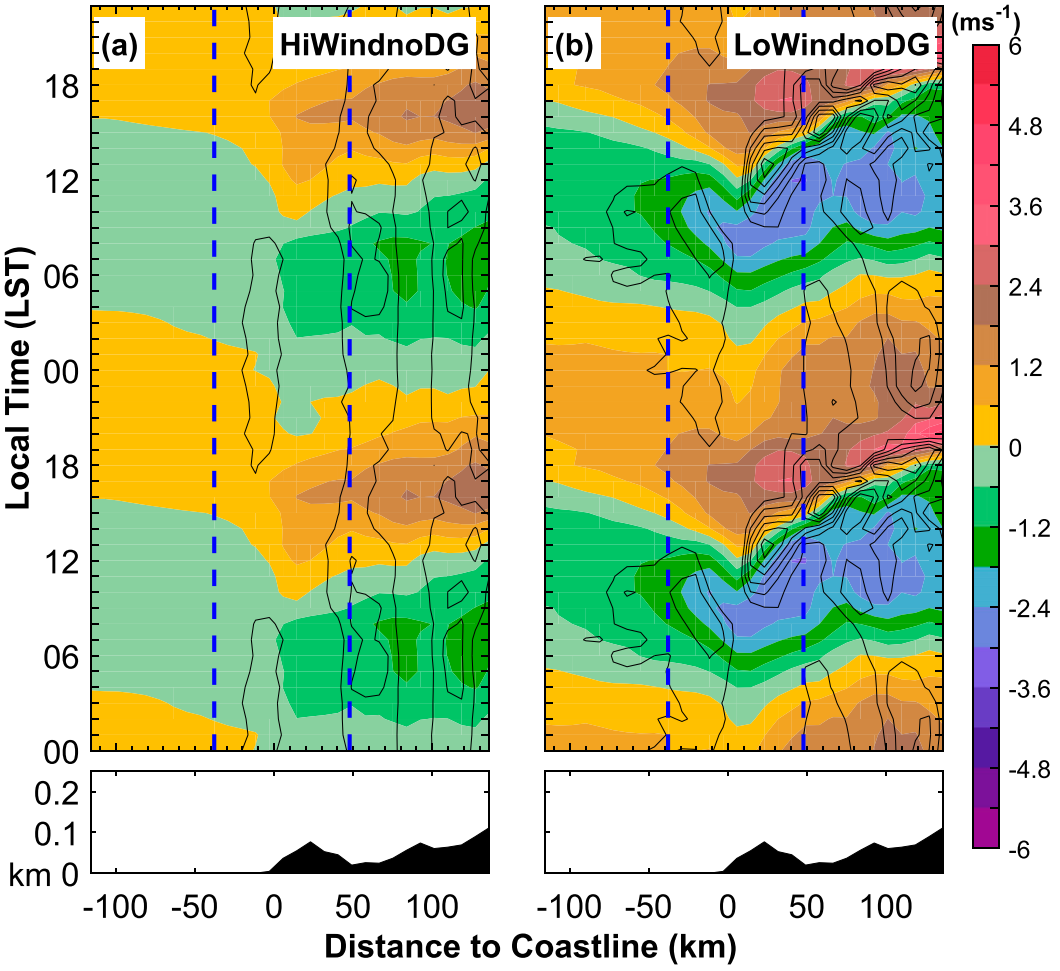

FIG. 12. As in Fig. 6, but for the (a) HiWindnoDG and (b) LoWindnoDG experiments.

friction on the land–sea breeze and its precipitation is limited (Fig. 12b).

Overall, the inland surface drag is crucial to the coastal rainfall in the high-wind days, while it has little influence on the coastal rainfall in the low-wind days. The related dynamical mechanisms can be explained as the wind perturbation created by the inland surface drag is a quadratic function of wind speed at reference levels. As a result, the effect of inland surface drag is much more significant during the high-wind days than that in the low-wind days. Under low-wind environment, the land–sea thermal contrast that drives the propagating land–sea breezes is the primary cause of the coastal rainfall, while the effect of inland surface drag is secondary.

4. Impacts of environmental moisture on coastal rainfall

In addition to the wind speed controls of the coastal rainfall mechanisms, the sensitivity of the accumulated coastal rainfall amount to the details of the atmospheric environment are further discussed in this section. First of all, the humidity fields in the high-wind and low-wind days are exchanged in experiments HiWindEXqv and LoWindEXqv to investigate the possible impacts of environmental moisture on the mechanisms responsible for the coastal rainfall. We can find that the spatial patterns of the accumulated rainfall are unchanged after the exchange of humidity fields (Figs. 13a and 13b). In HiWindEXqv, there still is a clear rainfall center along the coastline and obvious precipitation over the inland mountainous area (Fig. 13a). Meanwhile, the coastal rainfall is still weak in LoWindEXqv and a rainfall maximum can be found over the windward slopes of the northeast mountains (Fig. 13b). The similar rainfall spatial distributional patterns between HiWindEXqv (LoWindEXqv) and HiWind100 (LoWind100) suggest that the physical mechanisms responsible for the coastal rainfall patterns are not strongly sensitive to the environmental moisture variability during the south China

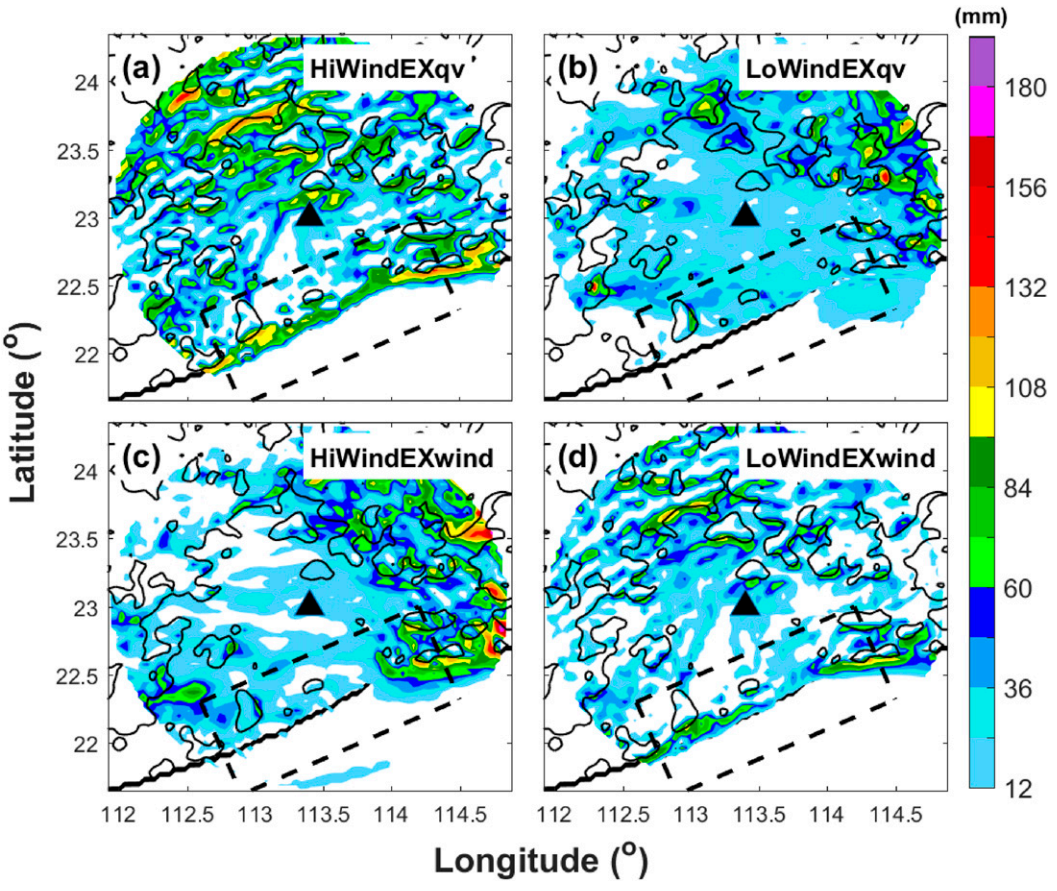

FIG. 13. As in Fig. 11, but for the (a) HiWindEXqv, (b) LoWindEXqv, (c) HiWindEXwind, and (d) LoWindEXwind experiments.

mei-yu period, while the ambient onshore wind speed should be the crucial factor controlling the coastal convective initiation. Nevertheless, under a drier environment, the accumulated rainfall amount over the coastal region is reduced by 24% in HiWindEXqv (Fig. 13a). On the other hand, the accumulated coastal rainfall amount is increased dramatically by 72% in LoWindEXqv (Fig. 13b) if supplied with moisture from the moister environment during high-wind days (Hiwind100).

To further prove the hypothesis that the ambient onshore wind speed is the crucial factor controlling the coastal rainfall pattern, another two sensitivity experiments HiWindEXwind and LoWindEXwind are conducted here. The wind fields in the high-wind and low-wind days are exchanged in the boundary conditions in these two experiments. In HiWindEXwind, after the winds in boundary conditions are reduced to that in the low-wind days, the rainfall center along the coastline shown in HiWind100 disappears. Instead, a rainfall maximum can be found over the northeast mountainous area and its adjacent coastal regions (Fig. 13c), which is similar with the rainfall spatial distribution pattern of LoWind100 (Fig. 3d). Because the environment is moister in the high-wind days, the rainfall intensity in HiWindEXwind is much stronger than that in LoWind100. On the other hand, after the winds in the boundary conditions are increased to that in the high-wind days, a clear rainfall center along the coastline appears in LoWindEXwind (Fig. 13d), which is similar with the coastal rainfall pattern of HiWind100 (Fig. 3c). However, the coastal rainfall intensity is much weaker in LoWindEXwind than that in HiWind100 owing to the dryer environment. In addition, coastal rainfall in HiWindEXwind shows an apparent diurnal propagation perpendicular to the coastline while the coastal rainfall in LoWindEXwind is quasi stationary with little propagation away the coastline (not shown here). These two sensitivity experiments further proved that the ambient onshore wind is the crucial factor controlling the diurnal variations and spatial distributions of the coastal rainfall, while the intensity of coastal rainfall is sensitive to the environmental moisture variability.

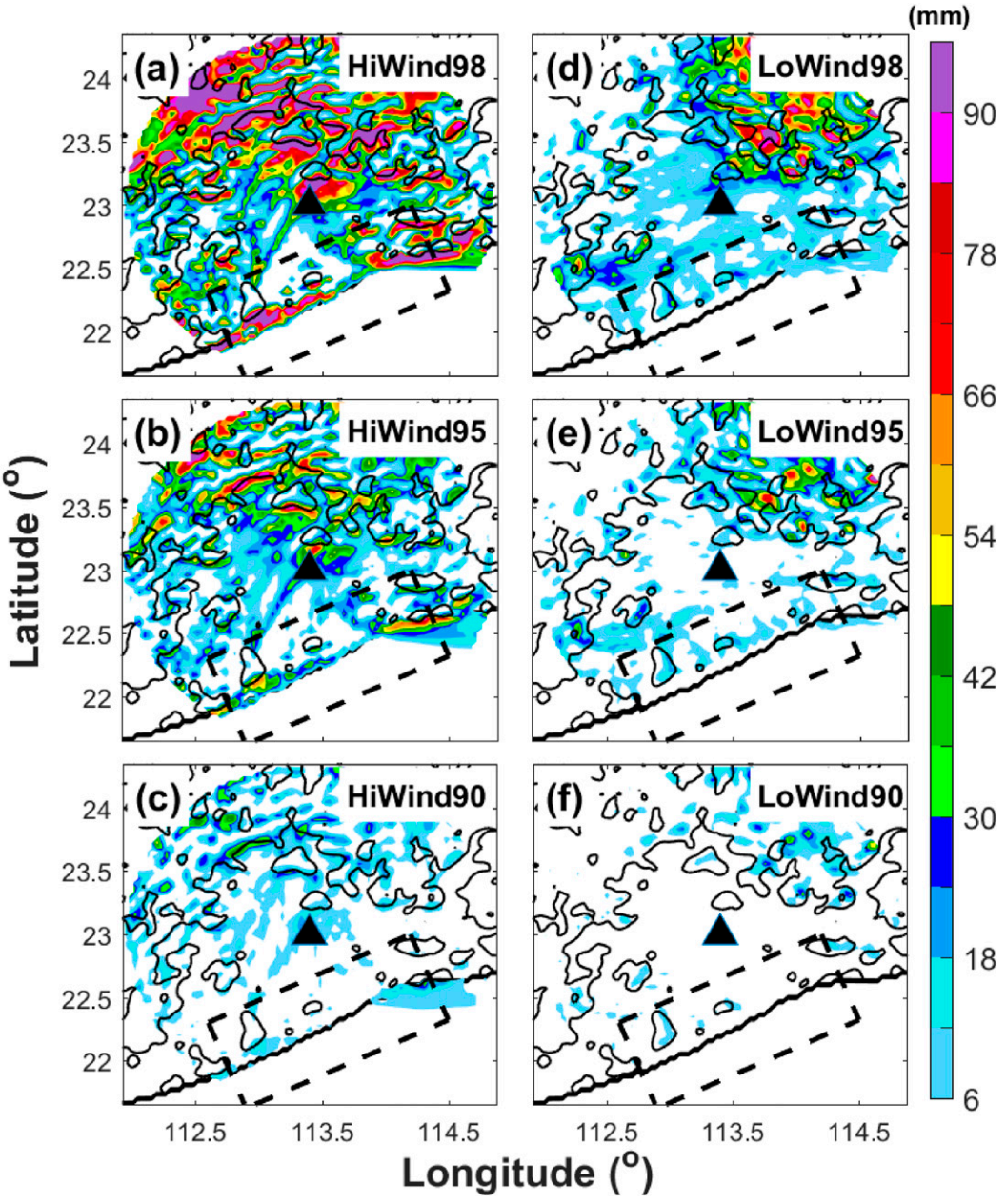

FIG. 14. Spatial distributions of average daily precipitation from (a) HiWind98, (b) HiWind95, (c) HiWind90, (d) LoWind98, (e) LoWind95, and (f) LoWind90 experiments. Orography is superimposed onto each panel and is shown as black contours that start from 100 m and have a 500-m interval. Coastal region of PRD is shown by the black dashed box.

To further investigate the sensitivity of accumulated coastal rainfall amount to the small perturbations in the incoming moisture. The water vapor flux on the lateral boundary is reduced to 98%, 95%, and 90% on all levels in HiWind98 (LoWind98), HiWind95 (LoWind95), and HiWind90 (LoWind90); the spatial distributions of the average daily rainfall for the final 9 days in these sensitivity experiments are shown in Fig. 14. Because the prevailing wind in the lower troposphere is southerly on average during the mei-yu seasons (Figs. 7a and 8a), the reduction of the water vapor flux on the lateral boundary means the moisture of the shoreward transporting air parcels from the ocean is reduced. We can find that in both the high-wind and low-wind days, the rainfall amounts over the coastal and inland mountainous regions are decreased with the decrease of incoming

moisture, while the spatial pattern of the rainfall is unaffected. In the high-wind days, the accumulated rainfall over the coastal region is reduced by 42%, 73%, and 93% when the water vapor flux on the lateral boundary is reduced to 98%, 95%, and 90%. Meanwhile, the coastal rainfall amounts in LoWind98, LoWind95, and LoWind90 are reduced by 37%, 67%, and 89%, respectively. Generally speaking, both the mechanically forced coastal rainfall in the high-wind days and the land–sea-breeze fronts that produce coastal rainfall during the low-wind days are sensitive to the moisture of the incoming flow from the ocean. Reduction of the incoming moisture flux from the ocean reduces the intensity of coastal convection and consequently reduces the total surface rainfall amount.

To further elucidate the impacts of incoming moisture on different levels on the accumulated coastal rainfall amount, a series sensitivity experiments HiWind98/0–1km (LoWind98/0–1km), HiWind98/2–3km (LoWind98/2–3km), and HiWind98/4–5km (LoWind98/4–5km) are conducted with the water flux on the lateral boundary reduced to 98% between 0 and 1, between 2 and 3, and between 4 and 5 km, respectively. The rainfall amount over the coastal region is reduced by 38% and 30% in HiWind98/0–1km and LoWind98/0–1km (Figs. 15a and 15d). Meanwhile, the coastal rainfall reductions in HiWind98/2–3km, LoWind98/2–3km, HiWind98/4–5km, and LoWind98/4–5km are all smaller than 3% (Figs. 15b,c,e,f). Results demonstrate that the coastal rainfall amounts under the strong and weak ambient onshore wind speeds are both sensitive to the incoming moisture in the boundary layer near the surface. The moisture in the lower and middle troposphere has little influence on the coastal rainfall accumulation. Considering that the moisture differences in the sensitivity experiments are comparable to the observational uncertainty in the low-level moisture, these results reflect an important limitation on the predictability of the rainfall over coastal regions of south China.

5. Summary and discussion

Complimentary to the previous radar–observational studies of C14 and C15 and modeling study of C16, this study investigates the influence of monsoonal wind speed and moisture content on the intensity and diurnal variations of the mei-yu season coastal rainfall over south China. Using high-resolution WRF simulations, particular emphasis is given to the impacts of the land–sea breeze, differential surface friction, and incoming oceanic moisture on the coastal rainfall under different environmental onshore wind strengths. Forty-two high-wind days and low-wind days are picked from the 2007–09 mei-yu seasons based on the daily average speed of the southerly wind at the 2-km altitude. The WRF idealized simulations with diurnally cyclic-in-time lateral boundaries verified well against the long-term radar observations, along with the realistic spatial distributions and diurnal variations of rainfall during the high-wind and low-wind days. The inland orographic rainfall intensity during the high-wind days in the WRF simulation is stronger than that in the radar observations, which may be induced by the model's inaccurate representation of atmospheric flow in the mountainous regions, deficiency in the model physics, the inadequate resolution, the modified coastline, and/or the underestimation of the radar QPE over the complex terrain.

Both the WRF simulations and radar observations show a prominent rainfall maximum along the coastline during the high-wind days. This costal rainfall center is quasi stationary and has little diurnal propagation perpendicular to the coastline (HiWind100). In contrast, the coastal rainfall is much weaker in the low-wind days, which propagates to the offshore direction from the night to the early morning and penetrates to the inland area from noon to the late afternoon (LoWind100). It is found that the coastal rainfall in the low-wind days is mainly produced by the land–sea-breeze fronts that propagate with the expansions of the land–sea breeze. Meanwhile, during the high-wind days, the initiation of coastal rainfall is closely related to the strong horizontal convergence on the coast, which is induced by the differential surface friction and the small coastal hills. This coastal convergence will be enhanced by the land breeze and produces stronger coastal precipitation during the early morning. Besides the rainfall, the ambient onshore wind speed also has prominent influences on the diurnal variations of the land–sea breeze. With a stronger land–sea temperature contrast, the land–sea-breeze circulations are much deeper and stronger during the low-wind days. Meanwhile, the establishment time of the land–sea breeze is earlier, and the inland propagating speed of the land–sea breeze is higher in the high-wind days. The offshore expansion of the land–sea breeze is later than its onshore expansion during the high-wind days, which can be explained as the offshore propagation of the land–sea breeze is suppressed by the strong environmental onshore wind during the high-wind days. Sensitivity experiments show that the differential surface friction has little influence on the strength of the land and sea-breeze fronts and their related rainfall intensity. As a result, the coastal rainfall is little affected by the modification of inland surface drag in the low-wind days (LoWindnoDG). However, at the high onshore wind speed, the total coastal rainfall amount reduced by more than 50% when the inland surface drag is set equal to

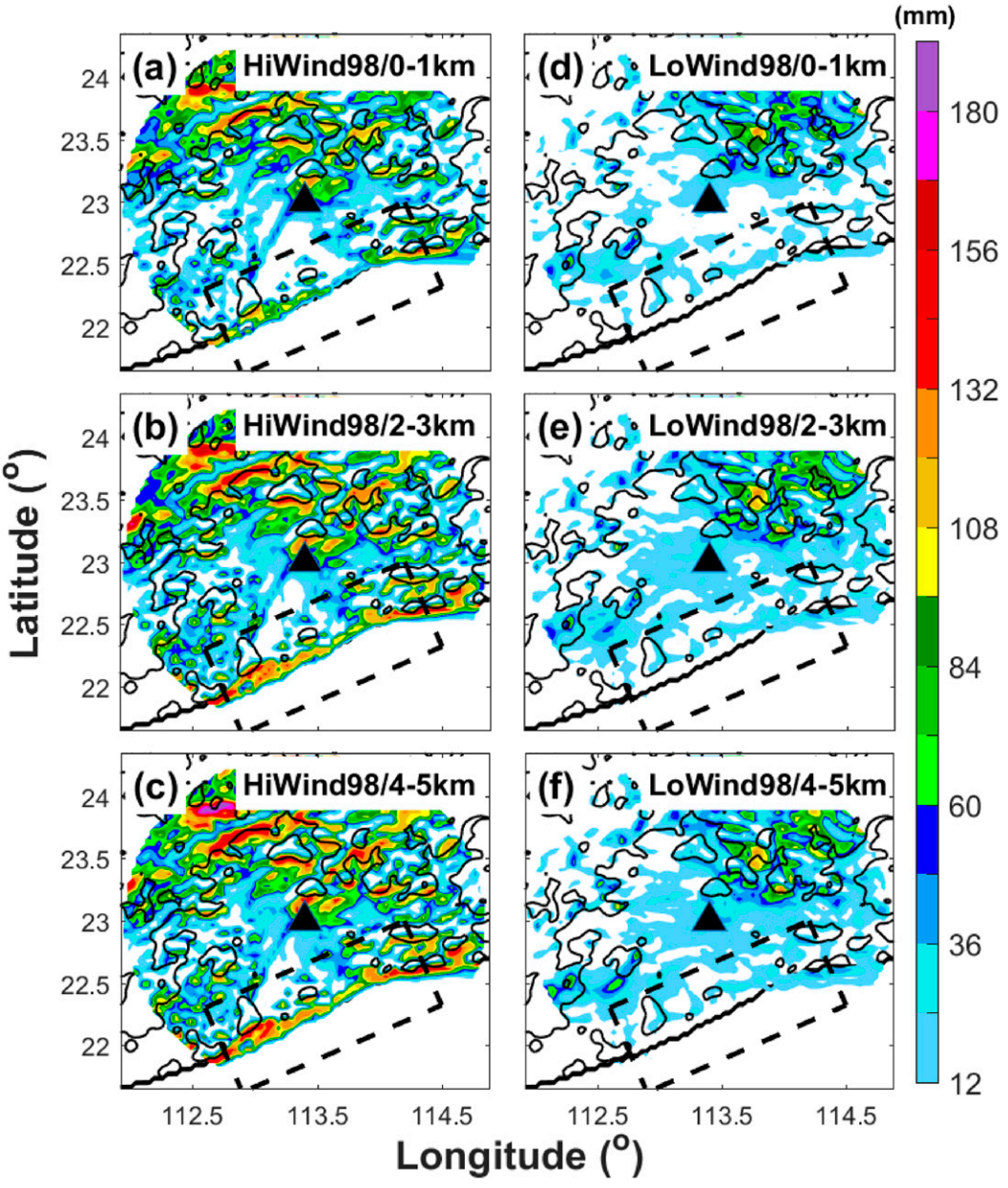

FIG. 15. As in Fig. 14, but for the (a) HiWind98/0–1km, (b) HiWind98/2–3km, (c) HiWind98/4–5km, (d) LoWind98/0–1km, (e) LoWind98/2–3km, and (f) LoWind98/4–5km experiments.

that over the ocean, which indicates that the convergence induced by the inland surface drag is crucial to the coastal rainfall accumulation in the high-wind days (HiWindnoDG).

The impacts of the environmental moisture on the coastal rainfall amount during the high-wind and low-wind days are further examined through a series of sensitivity experiments. HiWindEXqv and LoWindEXqv are two sensitivity experiments similar to HiWind100 and LoWind100 but with the humidity fields exchanged. Results show that the spatial distributions of the accumulated rainfall in HiWindEXqv and LoWindEXqv are still similar to that in HiWind100 and LoWind100, while the rainfall accumulation is decreased in HiWind100 and increased in LoWind100. It reaffirms the fact that the ambient onshore wind speed is the crucial parameter controlling the modes of coastal rainfall while the incoming moisture can influence the accumulated amount of rainfall. The hypothesis is further proved by the wind sensitivity experiments HiWindEXwind and LoWindEXwind. Additional sensitivity experiments with small perturbations in the environmental moisture show

that both the mechanically forced costal rainfall in the high-wind days and the land–sea breeze-produced coastal rainfall in the low-wind days are sensitive to the incoming moisture from the ocean, especially to the moisture in the boundary layer near the surface. The strong sensitivity of coastal rainfall accumulation to the moisture has implications for the predictability of extreme rainfall processes in the coastal region of south China.

In this paper, the initial and boundary conditions used in the simulations are the average of 42-day analysis of the high-wind and low-wind days over 3 years during the mei-yu seasons. In this situation, though different ambient wind speeds are considered, synoptic-scale variability, such as tropical cyclones and midlatitude fronts, are filtered out. The complex multiscale interactions between the monsoonal flow, synoptic systems, and the land–sea breeze and their impacts on the coastal rainfall still need further investigation, especially in a statistical sense. In addition, the moisture sensitivity experiments in this study only address a limited part of the predictability of the coastal rainfall over the region, and further works are still needed to examine the sensitivity of coastal rainfall to a broader range of environmental conditions. For example, the cloudiness, synoptic-scale wind direction, and pressure pattern also have considerable influences on the diurnal variations of the land–sea breeze and its related precipitation (Miller et al. 2003). Their possible effects under high-wind and low-wind conditions still deserve future studies.

Acknowledgments. The author Xingchao Chen is supported by the New York University in Abu Dhabi Research Institute under Grant G1102. This work was primarily supported by the National Fundamental Research 973 Program of China (2013CB430101), the Social Common Wealth Research Program (GYHY201006007), the National Natural Science Foundation of China (Grants 41275031 and 41322032), the Program for New Century Excellent Talents in Universities of China, and was also partially sponsored by NSF Grants 0904635 and 1114849. The author Xingchao Chen thanks the Department of Meteorology at Penn State University for hosting his visit. Computing was performed at the Texas Advanced Computing Center (TACC).

REFERENCES

Arritt, R. W., 1993: Effects of the large-scale flow on characteristic features of the sea breeze. *J. Appl. Meteor.*, **32**, 116–125, doi:10.1175/1520-0450(1993)032<0116:EOTLSF>2.0.CO;2.

Atkins, N. T., and R. M. Wakimoto, 1997: Influence of the synoptic-scale flow on sea breezes observed during CaPE. *Mon. Wea. Rev.*, **125**, 2112–2130, doi:10.1175/1520-0493(1997)125<2112:IOTSSF>2.0.CO;2.

Bao, X., and F. Zhang, 2013: Impacts of the mountain–plains solenoid and cold pool dynamics on the diurnal variation of warm-season precipitation over northern China. *Atmos. Chem. Phys.*, **13**, 6965–6982, doi:10.5194/acp-13-6965-2013.

Bechtold, P., J.-P. Pinty, and F. Mascart, 1991: A numerical investigation of the influence of large-scale winds on sea-breeze- and inland-breeze-type circulations. *J. Appl. Meteor.*, **30**, 1268–1279, doi:10.1175/1520-0450(1991)030<1268:ANIOTI>2.0.CO;2.

Chen, G., W. Sha, and T. Iwasaki, 2009: Diurnal variation of precipitation over southeastern China: Spatial distribution and its seasonality. *J. Geophys. Res.*, **114**, D13103, doi:10.1029/2008JD011103.

——, ——, M. Sawada, and T. Iwasaki, 2013: Influence of summer monsoon diurnal cycle on moisture transport and precipitation over eastern China. *J. Geophys. Res. Atmos.*, **118**, 3163–3177, doi:10.1002/jgrd.50337.

Chen, X., K. Zhao, and M. Xue, 2014: Spatial and temporal characteristics of warm season convection over Pearl River Delta region, China, based on 3 years of operational radar data. *J. Geophys. Res. Atmos.*, **119**, 12 447–12 465, doi:10.1002/2014JD021965.

——, ——, ——, B. Zhou, X. Huang, and W. Xu, 2015: Radar-observed diurnal cycle and propagation of convection over the Pearl River Delta during Mei-Yu season. *J. Geophys. Res. Atmos.*, **120**, 12 557–12 575, doi:10.1002/2015JD023872.

——, F. Zhang, and K. Zhao, 2016: Diurnal variations of the land–sea breeze and its related precipitation over south China. *J. Atmos. Sci.*, **73**, 4793–4815, doi:10.1175/JAS-D-16-0106.1.

Chien, F.-C., Y.-H. Kuo, and M.-J. Yang, 2002: Precipitation forecast of MM5 in the Taiwan area during the 1998 Mei-yu season. *Wea. Forecasting*, **17**, 739–754, doi:10.1175/1520-0434(2002)017<0739:PFOMIT>2.0.CO;2.

Colle, B. A., and S. E. Yuter, 2007: The impact of coastal boundaries and small hills on the precipitation distribution across southern Connecticut and Long Island, New York. *Mon. Wea. Rev.*, **135**, 933–954, doi:10.1175/MWR3320.1.

Dudhia, J., 1989: Numerical study of convection observed during the Winter Monsoon Experiment using a mesoscale two-dimensional model. *J. Atmos. Sci.*, **46**, 3077–3107, doi:10.1175/1520-0469(1989)046<3077:NSOCOD>2.0.CO;2.

Esteban, M. A., and Y.-L. Chen, 2008: The impact of trade wind strength on precipitation over the windward side of the island of Hawaii. *Mon. Wea. Rev.*, **136**, 913–928, doi:10.1175/2007MWR2059.1.

Gilmore, M. S., J. M. Straka, and E. N. Rasmussen, 2004: Precipitation uncertainty due to variations in precipitation particle parameters within a simple microphysics scheme. *Mon. Wea. Rev.*, **132**, 2610–2627, doi:10.1175/MWR2810.1.

He, H., and F. Zhang, 2010: Diurnal variations of warm-season precipitation over northern China. *Mon. Wea. Rev.*, **138**, 1017–1025, doi:10.1175/2010MWR3356.1.

Hong, S.-Y., J. Dudhia, and S.-H. Chen, 2004: A revised approach to ice microphysical processes for the bulk parameterization of clouds and precipitation. *Mon. Wea. Rev.*, **132**, 103–120, doi:10.1175/1520-0493(2004)132<0103:ARATIM>2.0.CO;2.

——, Y. Noh, and J. Dudhia, 2006: A new vertical diffusion package with an explicit treatment of entrainment processes. *Mon. Wea. Rev.*, **134**, 2318–2341, doi:10.1175/MWR3199.1.

Huang, W.-R., J. C. L. Chan, and S.-Y. Wang, 2010: A planetary-scale land–sea breeze circulation in East Asia and the western North Pacific. *Quart. J. Roy. Meteor. Soc.*, **136**, 1543–1553, doi:10.1002/qj.663.

Jiang, Z., D.-L. Zhang, R. Xia, and T. Qian, 2017: Diurnal variations of presummer rainfall over southern China. *J. Climate*, **30**, 755–773, doi:10.1175/JCLI-D-15-0666.1.

Klemp, J. B., J. Dudhia, and A. D. Hassiotis, 2008: An upper gravity-wave absorbing layer for NWP applications. *Mon. Wea. Rev.*, **136**, 3987–4004, doi:10.1175/2008MWR2596.1.

Luo, Y., H. Wang, R. Zhang, W. Qian, and Z. Luo, 2013: Comparison of rainfall characteristics and convective properties of monsoon precipitation systems over South China and the Yangtze and Huai River basin. *J. Climate*, **26**, 110–132, doi:10.1175/JCLI-D-12-00100.1.

Mapes, B. E., T. T. Warner, and M. Xu, 2003: Diurnal patterns of rainfall in northwestern South America. Part III: Diurnal gravity waves and nocturnal convection offshore. *Mon. Wea. Rev.*, **131**, 830–844, doi:10.1175/1520-0493(2003)131<0830:DPORIN>2.0.CO;2.

Melhauser, C., and F. Zhang, 2012: Practical and intrinsic predictability of severe and convective weather at the mesoscales. *J. Atmos. Sci.*, **69**, 3350–3371, doi:10.1175/JAS-D-11-0315.1.

Miller, S. T. K., B. D. Keim, R. W. Talbot, and H. Mao, 2003: Sea breeze: Structure, forecasting, and impacts. *Rev. Geophys.*, **41**, 1011, doi:10.1029/2003RG000124.

Mlawer, E. J., S. J. Taubman, P. D. Brown, M. J. Iacono, and S. A. Clough, 1997: Radiative transfer for inhomogeneous atmospheres: RRTM, a validated correlated-k model for the longwave. *J. Geophys. Res.*, **102**, 16 663–16 682, doi:10.1029/97JD00237.

Nugent, A. D., R. B. Smith, and J. R. Minder, 2014: Wind speed control of tropical orographic convection. *J. Atmos. Sci.*, **71**, 2695–2712, doi:10.1175/JAS-D-13-0399.1.

Qian, T., C. C. Epifanio, and F. Zhang, 2009: Linear theory calculations for the sea breeze in a background wind: The equatorial case. *J. Atmos. Sci.*, **66**, 1749–1763, doi:10.1175/2008JAS2851.1.

——, ——, and ——, 2012: Topographic effects on the tropical land and sea breeze. *J. Atmos. Sci.*, **69**, 130–149, doi:10.1175/JAS-D-11-011.1.

Rotunno, R., 1983: On the linear theory of the land and sea breeze. *J. Atmos. Sci.*, **40**, 1999–2009, doi:10.1175/1520-0469(1983)040<1999:OTLTOT>2.0.CO;2.

Ruppert, J. H., R. H. Johnson, and A. K. Rowe, 2013: Diurnal circulations and rainfall in Taiwan during SoWMEX/TiMREX (2008). *Mon. Wea. Rev.*, **141**, 3851–3872, doi:10.1175/MWR-D-12-00301.1.

Schumacher, R. S., 2015: Sensitivity of precipitation accumulation in elevated convective systems to small changes in low-level moisture. *J. Atmos. Sci.*, **72**, 2507–2524, doi:10.1175/JAS-D-14-0389.1.

Skamarock, W. C., and Coauthors, 2008: A description of the Advanced Research WRF version 3. NCAR Tech. Note NCAR/TN-475+STR, 113 pp., doi:10.5065/D68S4MVH.

Smith, R. B., and Coauthors, 2012: Orographic precipitation in the tropics: The Dominica Experiment. *Bull. Amer. Meteor. Soc.*, **93**, 1567–1579, doi:10.1175/BAMS-D-11-00194.1.

Sobel, A. H., C. D. Burleyson, and S. E. Yuter, 2011: Rain on small tropical islands. *J. Geophys. Res.*, **116**, D08102, doi:10.1029/2010JD014695.

Sun, J., and F. Zhang, 2012: Impacts of mountain–plains solenoid on diurnal variations of rainfalls along the mei-yu front over the east China plains. *Mon. Wea. Rev.*, **140**, 379–397, doi:10.1175/MWR-D-11-00041.1.

Trier, S. B., C. A. Davis, and D. A. Ahijevych, 2010: Environmental controls on the simulated diurnal cycle of warm-season precipitation in the continental United States. *J. Atmos. Sci.*, **67**, 1066–1090, doi:10.1175/2009JAS3247.1.

Tu, C.-C., Y.-L. Chen, C.-S. Chen, P.-L. Lin, and P.-H. Lin, 2014: A comparison of two heavy rainfall events during the Terrain-Influenced Monsoon Rainfall Experiment (TiMREX) 2008. *Mon. Wea. Rev.*, **142**, 2436–2463, doi:10.1175/MWR-D-13-00293.1.

Wang, H., Y. Luo, and B. J.-D. Jou, 2014: Initiation, maintenance, and properties of convection in an extreme rainfall event during SCMREX: Observational analysis. *J. Geophys. Res. Atmos.*, **119**, 13 206–13 232, doi:10.1002/2014JD022339.

Wang, S., and A. H. Sobel, 2017: Factors controlling rain on small tropical islands: Diurnal cycle, large-scale wind speed, and topography. *J. Atmos. Sci.*, https://doi.org/10.1175/JAS-D-16-0344.1, in press.

Wang, Y., J. Zhang, P.-L. Chang, C. Langston, B. Kaney, and L. Tang, 2016: Operational C-band dual-polarization radar QPE for the subtropical complex terrain of Taiwan. *Adv. Meteor.*, **2016**, 4294271, doi:10.1155/2016/4294271.

Xu, W., E. J. Zipser, and C. Liu, 2009: Rainfall characteristics and convective properties of mei-yu precipitation systems over South China, Taiwan, and the South China Sea. Part I: TRMM observations. *Mon. Wea. Rev.*, **137**, 4261–4275, doi:10.1175/2009MWR2982.1.

Yang, M.-J., B. J.-D. Jou, S.-C. Wang, J.-S. Hong, P.-L. Lin, J.-H. Teng, and H.-C. Lin, 2004: Ensemble prediction of rainfall during the 2000–2002 Mei-Yu seasons: Evaluation over the Taiwan area. *J. Geophys. Res.*, **109**, D18203, doi:10.1029/2003JD004368.

Yang, Y., Y.-L. Chen, and F. M. Fujioka, 2008: Effects of trade-wind strength and direction on the leeside circulations and rainfall of the island of Hawaii. *Mon. Wea. Rev.*, **136**, 4799–4818, doi:10.1175/2008MWR2365.1.

Zhang, Y., J. Sun, and S. Fu, 2014: Impacts of diurnal variation of mountain-plain solenoid circulations on precipitation and vortices east of the Tibetan Plateau during the mei-yu season. *Adv. Atmos. Sci.*, **31**, 139–153, doi:10.1007/s00376-013-2052-0.

Zhao, Y., 2014: Diurnal variation of rainfall associated with tropical depression in South China and its relationship to land-sea contrast and topography. *Atmosphere*, **5**, 16–44, doi:10.3390/atmos5010016.

Zheng, Y., M. Xue, B. Li, J. Chen, and Z. Tao, 2016: Spatial characteristics of extreme rainfall over China with hourly through 24-hour accumulation periods based on national-level hourly rain gauge data. *Adv. Atmos. Sci.*, **33**, 1218–1232, doi:10.1007/s00376-016-6128-5.

Zhong, S., and E. S. Takle, 1993: The effects of large-scale winds on the sea–land-breeze circulations in an area of complex coastal heating. *J. Appl. Meteor.*, **32**, 1181–1195, doi:10.1175/1520-0450(1993)032<1181:TEOLSW>2.0.CO;2.

Zhu, M., and B. W. Atkinson, 2004: Observed and modelled climatology of the land–sea breeze circulation over the Persian Gulf. *Int. J. Climatol.*, **24**, 883–905, doi:10.1002/joc.1045.